Heat transport by turbulent Rayleigh–Bénard convection for $Pr \simeq 0.8$ and $3 \times 10^{12} \lesssim Ra \lesssim 10^{15}$: aspect ratio $\Gamma = 0.50$

Guenter Ahlers[1,6,7]**, Xiaozhou He**[2,6]**, Denis Funfschilling**[3,6] **and Eberhard Bodenschatz**[2,4,5,6]

[1] Department of Physics, University of California, Santa Barbara, CA 93106, USA

[2] Max Planck Institute for Dynamics and Self-Organization (MPIDS), 37077 Göttingen, Germany

[3] LSGC CNRS - GROUPE ENSIC, BP 451, 54001 Nancy Cedex, France

[4] Institute for Nonlinear Dynamics, University of Göttingen, 37077 Göttingen, Germany

[5] Laboratory of Atomic and Solid-State Physics and Sibley School of Mechanical and Aerospace Engineering, Cornell University, Ithaca, NY 14853, USA

[6] International Collaboration for Turbulence Research

E-mail: guenter@physics.ucsb.edu

Abstract. We report on the experimental results for heat-transport measurements, in the form of the Nusselt number Nu, by turbulent Rayleigh–Bénard convection (RBC) in a cylindrical sample of aspect ratio $\Gamma \equiv D/L = 0.50$ ($D = 1.12$ m is the diameter and $L = 2.24$ m the height). The measurements were made using sulfur hexafluoride at pressures up to 19 bar as the fluid. They are for the Rayleigh-number range $3 \times 10^{12} \lesssim Ra \lesssim 10^{15}$ and for Prandtl numbers Pr between 0.79 and 0.86. For $Ra < Ra_1^* \simeq 1.4 \times 10^{13}$ we find $Nu = N_0 \, Ra^{\gamma_{\text{eff}}}$ with $\gamma_{\text{eff}} = 0.312 \pm 0.002$, which is consistent with classical turbulent RBC in a system with laminar boundary layers below the top and above the bottom

[7] Author to whom any correspondence should be addressed.

plate. For $Ra_1^* < Ra < Ra_2^*$ (with $Ra_2^* \simeq 5 \times 10^{14}$) γ_{eff} gradually increases up to 0.37 ± 0.01. We argue that above Ra_2^* the system is in the ultimate state of convection where the boundary layers, both thermal and kinetic, are also turbulent. Several previous measurements for $\Gamma = 0.50$ are re-examined and compared with our results. Some of them show a transition to a state with γ_{eff} in the range from 0.37 to 0.40, albeit at values of Ra in the range from 9×10^{10} to 7×10^{11} which is much lower than the present Ra_1^* or Ra_2^*. The nature of the transition found by them is relatively sharp and does not reveal the wide transition range observed in this work. In addition to the results for the genuine Rayleigh–Bénard system, we present measurements for a sample which was not completely sealed; the small openings permitted external currents, imposed by density differences and gravity, to pass through the sample. That system should no longer be regarded as genuine RBC because the externally imposed currents modified the heat transport in a major way. It showed a sudden decrease of γ_{eff} from 0.308 for $Ra < Ra_t \simeq 4 \times 10^{13}$ to 0.25 for larger Ra. A number of possible experimental effects are examined in a sequence of appendices; none of these effects is found to have a significant influence on the measurements.

Contents

IOP Institute of Physics Φ DEUTSCHE PHYSIKALISCHE GESELLSCHAFT

1. Introduction

In this paper we consider turbulent convection in a fluid contained between horizontal parallel plates and heated from below (Rayleigh–Bénard convection, or RBC; for reviews written for broad audiences see [1, 2]; for more specialized reviews see [3, 4]). The primary purpose of the work on which we report was to search for the transition to the 'ultimate' state of turbulent convection first predicted by Kraichnan [5] and Spiegel [6] half a century ago.

We focus on the particular case of a cylindrical sample of aspect ratio $\Gamma \equiv D/L = 0.50$ ($D = 1.12$ m and $L = 2.24$ m are the diameter and height respectively) because this particular geometry was used in previous searches for this state [7–17] and thus enables a more direct comparison with earlier measurements. Experiments searching for the ultimate state using other values of Γ are of course important as well and some have been carried out [17–22], but they are beyond the scope of this paper. The work reported here consists of measurements of the heat transport by the turbulent system. Other aspects will be discussed separately.

We present results that were obtained in the High-Pressure Convection Facility (the HPCF, a cylindrical sample of 1.12 m diameter) at the Max Planck Institute for Dynamics and Self-organization in Göttingen, Germany using sulfur hexafluoride (SF_6) at pressures up to 19 bar as the fluid. Early results from this work were presented in [23, 24, 26]. A description of the apparatus was given in [23]. This paper presents new results obtained after various sample-chamber modifications to be described in this paper and is a comprehensive report on this work. A brief report of these recent results was provided in [25].

The HPCF is located inside a pressure vessel known as the Uboot of Göttingen which gets filled with the gas of choice. Thus there must be some way for the gas to enter or leave the HPCF. Originally a small gap of average width about 1 mm was permitted for this purpose to remain between the top and bottom plate and the side wall of the sample [23]. Erroneously it was assumed that this gap was negligible because it is small compared to the 1120 mm sample diameter. This sample will be called the 'open' sample. It turned out that the results depended on the temperature difference between the fluid in the sample at a temperature T_m and the fluid in the remainder of the Uboot at T_U [26]. For that reason the HPCF was modified by sealing the bottom plate to the side wall, but leaving the gap between the top plate (TP) and the side wall open. This system will be called the 'half-open' sample. There still was a major difference between the results for $T_m > T_U$ and $T_m < T_U$, although these results differed from those of the closed sample. Thus, as a final measure, both the top and the bottom plates were sealed to the side wall, and a 25 mm diameter tube was installed to permit the gas to enter the HPCF. One end of the tube was flush with the inside of the side wall, and the other terminated in a remotely controlled valve. The sample could thus be filled while the valve was open, and then during measurements the valve could be closed. This sample will be called the 'closed' sample. Results for all three versions will be presented in this paper.

In the next section we shall define the parameters needed to describe this system (section 2). We shall then, in section 3, outline the main features of turbulent convection as they are now understood. First, in section 3.1, we describe the classical state of turbulent convection which exists below the transition to the ultimate state with turbulent boundary layers (BLs). This will be followed in section 3.2 by a description of what is known or expected for the ultimate state. This introductory material will be followed in section 4 by a brief discussion of the apparatus modifications used in this work. A detailed description of the main features was previously

presented [23]. Section 5 presents a comprehensive discussion of our results and of the results of others at large Ra for cylindrical samples with $\Gamma = 0.50$. It is followed by a summary of our work in section 6.

In a sequence of six appendices we discuss a number of experimental issues which might be of lesser interest to the general reader but which are of considerable importance to the specialist. First, in appendix A we compare measurements for three different angles of tilt of the sample axis relative to gravity. The effect of a tilt has been studied by several groups, with varying results [17, 27–31]. A tilt is used at times by experimentalists to give the large-scale circulation (LSC) in the sample a preferred azimuthal orientation. This was our motivation as well. We show that it had no discernible effect on Nu. In appendix B we demonstrate that non-Oberbeck–Boussinesq (NOB) effects [32, 33] have only a very minor effect on Nu which can be seen only at the largest values of ΔT near 20 K. In appendix C we present values of the parameter ξ introduced recently by Niemela and Sreenivasan [34] to describe a special NOB effect, which apparently occurs near critical points. We find that for our work $\xi \simeq 1.3$, indicating that the effect discussed in [34] (which occurs for small or negative ξ) is not expected to be relevant to our study. In appendix D we provide the results for the horizontal temperature variations in the top and bottom plate of the sample and demonstrate that they do not influence the measured values of Nu. In appendix E we show that the 'closed' sample really was completely sealed. In appendix F we present data for the influence of a mismatch between the temperature of the sample side shield (SS) and the sample mean temperature T_m, and show that the SS temperature-regulation is good enough for these effects to be negligible. Finally, in appendix G, we give a complete list of our data in numerical form.

2. The system parameters

For turbulent RBC in cylindrical containers there are two parameters which, in addition to Γ, are expected to determine its state. They are the dimensionless temperature difference, as expressed by the Rayleigh number

$$Ra \equiv \frac{\alpha g \Delta T L^3}{\kappa \nu}, \tag{1}$$

and the ratio of viscous to thermal dissipation, as given by the Prandtl number

$$Pr \equiv \nu/\kappa. \tag{2}$$

Here α is the isobaric thermal expansion coefficient, g the gravitational acceleration, κ the thermal diffusivity, ν the kinematic viscosity, and $\Delta T \equiv T_\mathrm{b} - T_\mathrm{t}$ the applied temperature difference between the bottom (T_b) and the top (T_t) plate.

In this paper we present measurements of the heat transport. These results are presented in the form of the scaled effective thermal conductivity, known as the Nusselt number, which is given by

$$Nu \equiv \frac{QL}{A \Delta T \lambda}. \tag{3}$$

Here Q is the applied heat current, $A = D^2\pi/4$ the sample cross-sectional area, and λ the thermal conductivity. The measurements cover the range $3 \times 10^{12} \lesssim Ra \lesssim 10^{15}$ and are for Pr ranging from 0.79 at the lowest to 0.86 at the highest Ra.

All fluid properties needed to calculate Ra, Pr, and Nu were evaluated at the mean temperature $T_m = (T_t + T_b)/2$ of the sample. They were obtained from numerous papers in the literature, as discussed in [35].

3. The characteristics of turbulent Rayleigh–Bénard convection

3.1. The classical state

A 'classical' state of RBC exists below a transition *range* to an 'ultimate' state; the transition range extends over more than a decade, approximately from Ra_1^* to Ra_2^* [25]. For simplicity of discussion we shall characterize this range by Ra^*, taken to lie perhaps somewhere near the middle of the range, which, for the parameters of our work, is about 10^{14} [25, 36]. For $Ra \lesssim Ra^*$ the heat transport in this system is controlled by laminar thermal BLs, one just below the top and the other just above the bottom plate. The value of Ra^* has been the subject of discussion for some time, and a major issue at the forefront of the field is the nature of the state above Ra^*. Estimates of Ra^* are not very accurate; a reasonable argument [36] yielded $Ra^* \simeq 10^{14}$ or so for $Pr \simeq 1$, although another estimate [19] gave a value closer to 10^{12}.

For $Ra < Ra^*$ nearly half of ΔT is found across each BL, and the sample interior (known as the 'bulk') has a highly fluctuating temperature which is nearly uniform in the time average [37, 38]. At a more detailed level it was recognized long ago that the bulk actually sustains small temperature gradients, but the total temperature drop across it is much smaller than that across the BLs (see, for instance, [39–41]). Very recently it was found that these small temperature variations in the bulk take the form of a logarithmic dependence on the distance from the plates [42].

For the classical state it is well established both experimentally [18, 43–48] and theoretically [36, 49–51] that the Nusselt number can be represented by a power law

$$Nu = N_0 Ra^{\gamma_{\text{eff}}} \tag{4}$$

with the effective exponent varying from about 0.28 near $Ra = 10^8$ to about 0.32 near $Ra = 10^{11}$, at least when Pr is close to one or larger.

It is also well established that, in cylinders with $\Gamma \simeq 0.5$ containing a fluid with $Pr \simeq 0.7$ and for $Ra \lesssim 10^{11}$, there is a LSC in the sample interior that takes the form of a single convection roll, with up-flow along the side wall at an azimuthal position θ_0 and down-flow also along the wall but at an azimuthal position close to $\theta_0 + \pi$ [41, 52]. The LSC is bombarded by the small-scale fluctuations of the system, and may be regarded as a stochastically driven system that fluctuates intensely [53, 54]. Even at modest Ra below, say, 10^{11} and for Pr near 0.7, the LSC existence is intermittent [52]. It frequently collapses, only to re-form again at a somewhat later time. Whether the LSC survives at all up to Ra^* had not been clear heretofore; it was recognized (see, for instance, [19]) that the LSC becomes less well defined as Ra increases, but concrete quantitative experimental evidence for its existence or demise has only become available during this work [25]. We found that, even for $Ra = 10^{15}$, there is evidence of its existence, but its average lifetime is short and it may be regarded more appropriately as just one of the continuum of modes contributing to the fluctuation spectrum of the system. This will be reported in detail in a subsequent paper.

When the fluctuations are not too vigorous, the LSC due to its horizontal flow with speed U just adjacent to the top and bottom plate will establish *viscous* BLs adjacent to the plates.

The viscous BLs may be imbedded in the thermal ones or vice versa, depending on Pr. These BLs are laminar, albeit fluctuating [55, 56], in the classical state.

3.2. The ultimate state

About half a century ago it was predicted by Kraichnan [5] and Spiegel [6] that, in the absence of BLs, the Nusselt number should be proportional to Ra^γ with $\gamma = 1/2$. This prediction is consistent with rigorous upper bounds for $Nu(Ra)$ obtained by Howard [57] and by Doering and Constantin [58]. Although it seems difficult to construct a physical system without boundaries, the $\gamma = 1/2$ prediction was supported by direct numerical simulations (DNS) of RBC with periodic boundary conditions in the vertical direction and forcing in the bulk [59–61], as well as by DNS for the Rayleigh–Taylor instability [62], which is expected to reveal similar phenomena and has no boundaries. Experimentally, it is noteworthy that a *local* heat-flux measurement in the center of a Rayleigh–Bénard sample in the classical state (i.e. in the state with laminar BLs) yielded an exponent of 0.5 [63], even though the global heat flux led to $\gamma_{\text{eff}} \simeq 0.3$.

In the presence of boundaries, Kraichnan noted that the BLs should become turbulent when Ra exceeds some characteristic value Ra^*. This event was expected to be induced by the shear applied to the BLs by the LSC, or if none exists, by the vigorous turbulent fluctuations in the sample interior. It was expected to occur when a shear Reynolds number Re_s exceeds a characteristic value Re_s^*, which is expected to be somewhere in the range from about 200 to 400 [36, 64, 65]. The shear Reynolds number in turn is expected to be related to the bulk Reynolds number Re by $Re_s = a\sqrt{Re}$, where a is a constant that was estimated to be close to 0.5 [36]. Significant uncertainty prevails about the appropriate estimate of $Re(Ra)$. At modest Ra one expects it to be determined primarily by the horizontal component of the LSC velocity just above the BL. In that case (and for $\Gamma = 1$) it is expected to be given, with reasonable reliability, by the Grossmann–Lohse model [36]. However, at the values of Ra relevant here the LSC velocity is highly intermittent, its time average is small, and the root-mean-square fluctuation velocity is an order of magnitude larger [25]. When fluctuations dominate, their root-mean-square horizontal velocity near the BLs should yield a measure of the applied shear. In that case the characteristic size of fluctuations will cover a range, roughly from D down to smaller lengths, and will be intermittent in time. One would then expect the turbulent shear layers to be more localized laterally in space, as well as in time. In view of the complex phenomena we have just described, any estimate of Ra^* can only be expected to hopefully be of the right order of magnitude. We note that the Grossmann–Lohse model, with parameters determined by fits to experimental data for $\Gamma = 1$ and at much smaller Ra, yields $Ra^* \simeq 10^{14}$ when $Pr \simeq 1$. It predicts that Ra^* increases with Pr (see figure 9 and equation (5) below).

In Kraichnan's considerations he assumed that the viscous and thermal BLs would undergo the shear-induced transition at the same value of Ra. Even in the presence of rigid top and bottom plates the prediction for the large-Ra asymptotic state then was still $Nu \sim Ra^{1/2}$. However, Kraichnan [5] predicted that, due to the turbulent BLs, there would be logarithmic corrections to this power law. Recently Grossmann and Lohse considered the possibility that the thermal and viscous BLs may undergo the turbulent shear transition at different values of Ra or simultaneously, and derived the consequences of transitions in one or the other or both [65]. The ultimate state would then correspond to the case where both the viscous and the thermal BLs become turbulent (see section 3.3 of [65]; we will reserve the notation Ra^* for this case).

In an analogy to the logarithmic velocity profiles in turbulent shear flows first considered by von Kármán [66] and Prandtl [67] (for a recent review, see [68]), Grossmann and Lohse [65] predicted that the turbulent BLs would extend throughout the sample, replacing the bulk by a temperature profile that varies logarithmically with the distance from the plates. For the Boussinesq system [32, 33] the two profiles, one coming from the top and the other from the bottom plate, would then meet at the horizontal mid-plane of the cell. Logarithmic temperature profiles have indeed been observed in recent measurements for the ultimate state [42]; but since they were found for the classical state as well, it remains unclear to what extent this finding supports the prediction. In conjunction with the viscous and thermal sublayers near the plates (which survive above Ra^* because of the boundary conditions at the solid–fluid interface), the extended turbulent BLs lead to logarithmic corrections to the asymptotic power law for Nu. The Grossmann and Lohse prediction for these logarithmic corrections differs from the original form of the logarithms given by Kraichnan. However, for either prediction the corrections vary only slowly with Ra, and in experimentally accessible Ra ranges one expects an effective power law with an effective exponent $\gamma_{\text{eff}} \simeq 0.38$–$0.40$. The asymptotic regime where the effective exponent has essentially reached 1/2 is well out of reach of any conceivable experiment.

A notable recent success in the search for the ultimate state has been achieved with turbulent Couette–Taylor (CT) flow [69, 70] (it had been shown on the basis of its equations of motion that it should undergo an ultimate-state transition that is analogous to that of RBC [71]). In the CT case the shear is applied directly to the fluid by concentric rotating cylinders, and thus is much more effective in driving the BLs into the turbulent state than is the shear in RBC, which is generated as a secondary effect by the buoyancy-induced LSC or the fluctuations. The CT measurements yielded an effective exponent of 0.38 for the corresponding variables, consistent with 1/2 and the predicted logarithmic corrections [65].

For RBC the situation is less clear. In order to reach exceptionally high Ra, two groups used fluid helium near its critical point at temperatures of about 5 K and pressures of about 2 bar. One of them [9, 12], at the time located at Grenoble, reported to have found the ultimate regime, and cited a value $Ra^* \simeq 10^{11}$. We shall refer to these results as the 'Grenoble' data. A major puzzle created by these results is that one can estimate that the data imply $Re_{\text{s}}^* \simeq 100$ or less; this seems too low for any BL shear instability.

In a second nominally equivalent investigation near the critical point of helium Niemela *et al* [10] made measurements of Nu up to $Ra \simeq 10^{17}$. They found that $Nu \propto Ra^{0.32}$ [72] up to their largest Ra, without any evidence for a transition. This work was done at the University of Oregon, and we shall refer to these results as the 'Oregon' data. In this case the absence of a transition does not necessarily contradict expectations because Pr began to increase as Ra exceeded about 10^{13}, and it is plausible that $Ra^*(Pr)$ was never reached or resolved in that experiment.

There have been a number of additional low-temperature experiments intended to clarify the situation; we refer to a recent review [3] for a detailed discussion of these measurements. For completeness we mention a comprehensive recent article by Roche *et al* [17] which examines the influence of the nature of the side walls, of Γ, of Pr, and of several other factors which seem to influence the transition to a state with γ_{eff} significantly larger than 0.32. This survey concludes that a transition to the ultimate regime occurs in several experiments, but again these transitions occurred at unexpectedly low values of Ra. The survey concludes that the transition occurs at smaller Ra when Pr is larger, which is opposite to the Pr dependence of Ra^* expected for the shear instability. Since no LSC-induced shear instability is likely to have occurred, and since

Table 1. Versions of the HPCF. The second column gives the material used to construct the top and bottom plates. The third column indicates whether the top and/or bottom plate were sealed to the side wall. The fourth column gives the numbers of the runs performed in each unit.

Version	Plates	Seals	Runs
HPCF-I	Aluminum	None	080827–090313
HPCF-IIa	Copper	None	090505–090917
HPCF-IIb	Copper	None	090905–100125
HPCF-IIc	Copper	Bottom	100202–100502
HPCF-IId	Copper	Bottom and top	100612–100818
HPCF-IIe	Copper	Bottom and top	100918–110919
HPCF-IIf	Copper	Bottom and top	120224–120429
HPCF-IIg	Copper	Bottom and top	120713 etc

the ultimate-state predictions are based on the assumption of turbulent BLs, it remains unclear to us how the states with γ_{eff} much larger than 0.32 reported in [17] are related to the Kraichnan prediction [5] or to the states discussed by Grossmann and Lohse [65].

4. Apparatus

Versions HPCF-I, HPCF-IIa, and HPCF-IIb of the apparatus were described in detail in [23]. A schematic diagram of these units can be found in figure 2 of that reference. HPCF-I had aluminum top and bottom plates, whereas HPCF-II had copper plates. HPCF-IIa and IIb differed only in the amount and type of insulation (mostly open-pore foam and aluminum-coated polyester film, see [23]) provided outside the sample cell, and the data obtained with them showed no obvious differences. More recently five additional modifications, known as HPCF-IIc to -IIg, were developed; corresponding schematic diagrams are shown in figure 1. HPCF-IId and later versions differed from HPCF-IIc by the 2.5 cm diameter side arm and valve used to fill and empty the sealed samples, and by whether or not the side wall was sealed to the bottom and/or TP. Further, starting with HPCF-IId, the additional micro-shield BBMS, located 5 mm above BMSt, was in place. Its temperature was servoed at T_m. HPCF-IId failed because pressurization of the Uboot at too fast a rate had caused a pressure differential between the Uboot and the sample, which was large enough (over 0.05 bar) to lift the 500 kg bottom-plate composite and thus destroy the seal to the side wall. The data obtained with it are thus not useable. HPCF-IIe is a repaired version identical to IId. HPCF-IIf had two additional columns of thermistors, eight each, installed in its bottom half in the sample interior at a distance of 1 cm from the side wall. It was used for the work reported in [42]. HPCF-IIg had more additional vertical columns of thermistors installed at various radial positions and is intended for future work. Table 1 lists the major differences between the eight versions, as well as the identifications of the runs[8] performed in each.

　　All samples had an internal height $L = 2240 \pm 2$ mm and diameter $D = 1122 \pm 2$ mm. The measurements to be discussed here were made in HPCF-IIb to -IIe. All samples had a Plexiglas

---

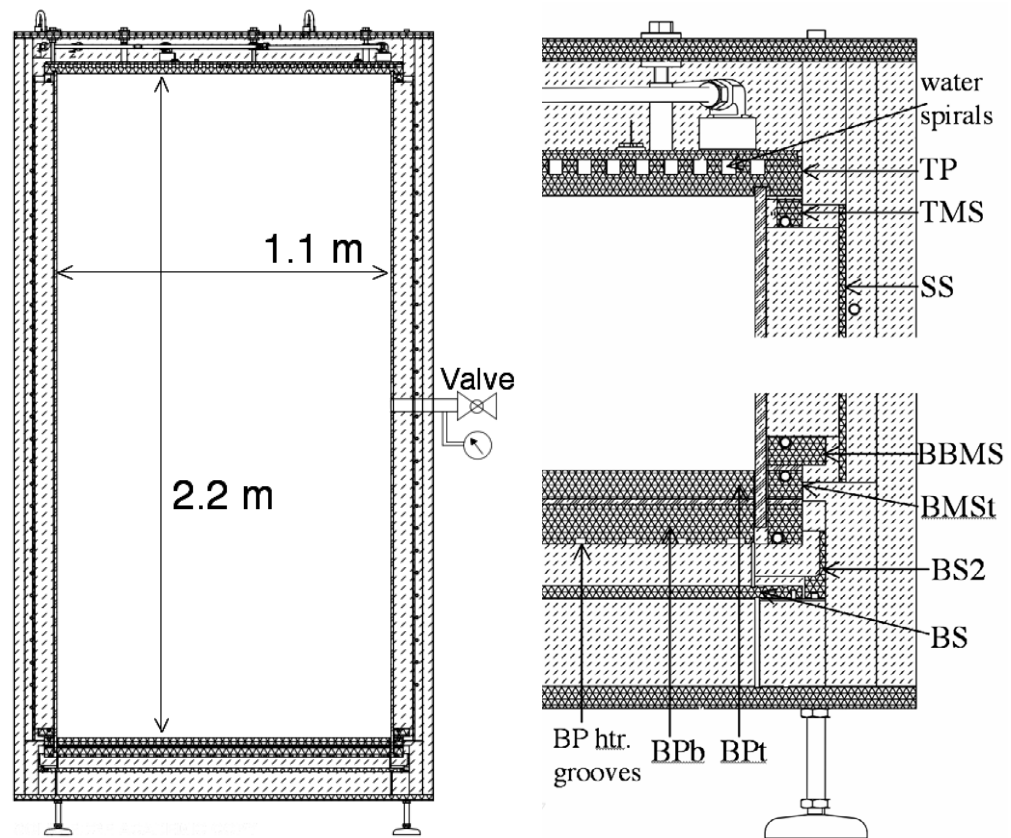[8] The run numbers had the structure 'yymmdd'.

Figure 1. Left: diagram of HPCF-IIe. Right: detailed diagram of the top and bottom corners of HPCF-IIc to HPCF-IIe. All parts are shown to scale, except for the valve in the left part. We refer to figure 2 of [23] for a description of many features that were common with HPCF-I to HPCF-IIb. The bottom plate was a composite consisting of a bottom member 'BPb', a top member 'BPt', and a Lexan sheet between them. The bottom-plate heater was imbedded in epoxy inside the heater grooves ('BP htr grooves'). The bottom shield ('BS') was extended by adding a section ('BS2'). The bottom bulk microshield ('BBMS'), servoed at T_{m}, is new. The side shield ('SS') and top microshield ('TMS') are unchanged. The location and size of the spiral water channels ('water spirals') in the top plate ('TP') are indicated.

side wall of 0.95 cm thickness and several thermal shields. The entire sample was immersed in a high-pressure vessel, known as the Uboot of Göttingen, that could be filled with various gases, including sulfur hexafluoride (SF_6), up to a pressure of $P = 19$ bar. As shown in figure 1, all samples had a composite bottom plate consisting of a bottom (BPb) and a top (BPt) member made of copper (aluminum for HPCF-I) and a 5 mm thick layer of Lexan sandwiched between them. The composite was glued together with very thin layers of degassed Stycast 1266 epoxy. The temperature difference across this composite, together with the composite conductance, was used to infer the heat current Q that entered the sample at the bottom. The underside of the bottom member of the composite was heated electrically by a heater immersed in epoxy in grooves ('BP htr grooves'). The TP was cooled by a water circuit consisting of two pairs

IOP Institute of Physics **Ⓓ** DEUTSCHE PHYSIKALISCHE GESELLSCHAFT

of double spirals. The pairs were in parallel, and the flows in the two members of a given pair were anti-parallel. Remaining horizontal thermal gradients in the TP and the BPt are discussed in appendix D.

The various shields which prevented parasitic heat losses from the sample cell were discussed in detail in [23]. Starting with HPCF-IId we added two more shields. The bottom shield, which is always servoed at the temperature of the bottom member BPb of the composite, was extended by adding the section BS2 (see figure 1). A more significant addition was the 'Bottom Bulk Micro Shield' BBMS. It was servoed at T_{m} and thus minimized vertical thermal gradients in the space between the side wall and the SS. Prior to the addition of BBMS there was a vertical temperature drop from the BPt temperature at BMSt to T_{m} at TMS, which is approximately equal to $\Delta T/2$ and thus generated a Rayleigh number about equal to half the sample Ra. Even though the space between the side wall and the SS was filled with foam and polyester film, convection is believed to have been induced in this space during runs at the larger values of Ra.

HPCF-IIc was identical to HPCF-IIb, except that a seal consisting of silicone adhesive was applied to the inside corner between the side wall and the top of the bottom-plate composite along the entire periphery. It is expected that this seal will prevent any flow through the small gap, of width about 1 mm, between the side wall and the bottom plate. A similar gap between the side wall and the TP was left open since fluid had to be allowed to enter or leave the cell as the temperature or pressure was changed.

HPCF-IId to HPCF-IIg consisted of a completely sealed system, with no gaps between the top or bottom plates and the side wall. A tube of inside diameter 2.5 cm was installed and entered the side wall at half height. Its termination was flush with the inside of the side wall, without any protrusion into the convection chamber. Outside the convection chamber this tube contained a remotely operated ball valve. A small-diameter ($\simeq 3$ mm) tube led from the sample side of the 2.5 cm diameter tube to a location outside the Uboot where it was connected to the pressure gauge. Thus, the actual sample pressure could be monitored. At each set point of the experiment the system was equilibrated with the valve open for about six hours. The valve was then closed, permitting measurements on a completely sealed system. The fill tube had two side arms with an additional valve in each. One opened when the pressure difference $P_{\mathrm{U}} - P$ between the Uboot and the sample exceeded 25 mbar; the other opened when this pressure difference was less than -25 mbar. We note that a pressure difference of 25 mbar leads to a force of about 250 kg acting on the top and bottom plates. When for instance this force exceeds the weight of the TP, then this plate will lift up and damage will be done to the instrument. In order to keep $|P_{\mathrm{U}} - P|$ sufficiently small, filling and emptying of the Uboot and sample was done very slowly, over a period of a day or two depending on the desired pressure. Measurements of the sample pressure under various conditions showed that the sample was indeed sealed, as discussed in appendix E.

Nusselt-number measurements were based on temperatures determined with fifteen thermometers, five each in the two members BPb and BPt of the bottom-plate composite and five in the TP. Each set of five consisted of one thermometer placed at the plate center and four, positioned equally spaced azimuthally, at a distance of $0.42D$ from the center. The thermometers in the BPt and the TP were located about 1 mm from the fluid–copper interface. The three sets of five thermometers were used to obtain the averages T_{BPb}, T_{BPt}, and T_{TP}. T_{BPb} and T_{BPt} were used to calculate the heat current entering the sample. T_{BPt} and T_{TP} were used to obtain ΔT and Ra. In a typical run both T_{BPb} and T_{TP} were regulated at a specified setpoint.

A small correction to Nu was made for the sidewall conductance [73, 74]. This correction was about 1.4% for $Ra \simeq 10^{15}$ and about 3.5% for $Ra \simeq 5 \times 10^{12}$. Neglecting this correction changed the exponent obtained from a power-law fit to the data for $Nu(Ra)$ by about -0.003. Estimates and a comparison of measurements with copper and aluminum plates [75] showed that corrections for the finite conductivity of the top and bottom plates [76, 77] were negligible.

5. Results

5.1. Closed sample

5.1.1. The broad overview. In this subsection we present the results for the closed sample HPCF-IIe which is our best approximation to the idealized RB system. In section 5.2 we compare these results with previous measurements. Then, in section 5.3, we discuss the measurements for the open sample where the RB system may be perturbed by an additional current entering or leaving the sample through the narrow gap between the top and bottom plates and the side wall because of the chimney effect. Finally, in section 5.4, we consider the case where only the bottom of the sample is sealed (HPCF-IIc) while a gap remains between the TP and the side wall (the 'half-open' sample).

Results of the Nu measurements for the closed sample (HPCF-IIe) were reported briefly before [25]. It was found that they depended slightly on $T_m - T_U$, but much less so than the data for the open or the half-open sample. We have been unable to determine the reason for this dependence which persisted in spite of the many thermal shields and the foam and foil insulation that were provided (see [23], and section 4 and figure 1 above).

In figure 2 we show Nu as a function of Ra with both axes on a logarithmic scale. The open circles are for $T_m - T_U \gtrsim 2\,\mathrm{K}$, and the solid black circles represent the data for $T_m - T_U \lesssim -2\,\mathrm{K}$. Within the resolution of this figure the open and solid circles are seen to agree quite well with each other and with the Oregon data (red stars), although small differences can be noticed on close inspection. Both our data sets and the Oregon data differ significantly from the Grenoble data (open blue circles). A more detailed comparison with those as well as with other [17, 78] results is given below.

5.1.2. The classical state. First we examine $Nu(Ra)$ in the classical regime in greater detail. Figure 3 is a high-resolution graph of the data in this parameter range in the form of $Nu/Ra^{0.312}$ on a linear scale as a function of Ra on a logarithmic scale. One sees that each of the two data sets covers a range of about a decade in the classical regime where a simple power law describes them well. A fit of the power law equation (4) to the data points that are indicated by small red dots in their centers gave the parameter values and standard errors (67% confidence limits) listed in table 2. On the basis of this analysis we chose $\gamma_{\mathrm{eff}} = 0.312$ as our best estimate of the effective exponent in the classical regime. As can be seen from the table, the uncertainty of this result due to the scatter in the data is less than 0.001. We estimate that an additional uncertainty comes from possible systematic errors of the sidewall correction, and thus the overall uncertainty of the exponent is about 0.002. This value is consistent with numerous other measurements at smaller Ra and larger Pr, and agrees quite well with the value 0.323 obtained from a numerical analysis of the Grossmann–Lohse model, equations (13) and (14) of [50], for $10^{12} \simeq Ra \simeq 10^{13}$
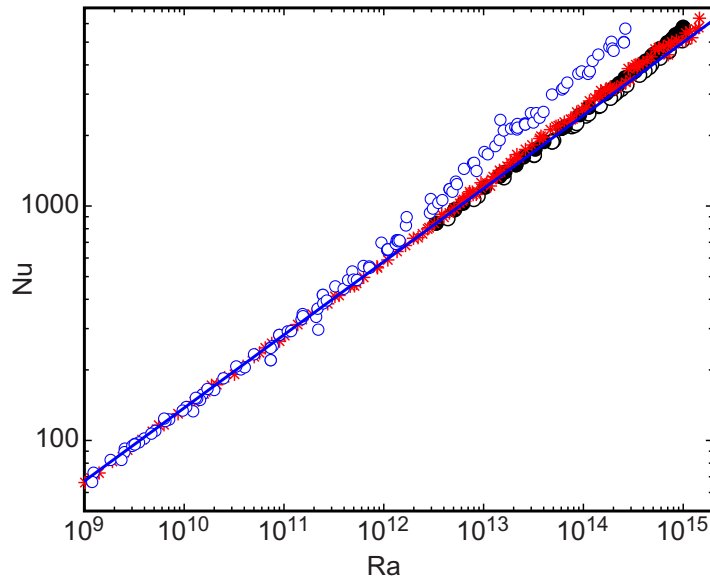
Figure 2. The Nusselt number Nu as a function of the Rayleigh number Ra on logarithmic scales. Solid black circles: this work, $T_m - T_U < -2\,\mathrm{K}$. Open black circles: this work, $T_m - T_U > 2\,\mathrm{K}$. Red stars: the Oregon data [10, 11, 72]. Open blue circles: the Grenoble data [9, 12]. Blue solid line: the power law $Nu = 0.1044 Ra^{0.312}$.
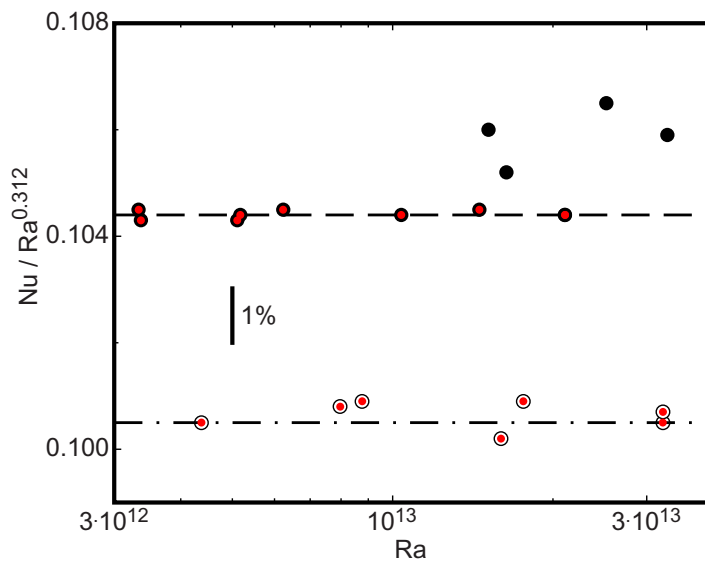
Figure 3. The reduced Nusselt number $Nu/Ra^{0.312}$ on a linear scale as a function of Ra on a logarithmic scale. Solid (open) black circles: $T_m - T_U < -2\,\mathrm{K}$ ($T_m - T_U > 2\,\mathrm{K}$). The points indicated by a red dot in the center were used in a least-squares fit of a power law to the data.

and $Pr = 0.8$ (but for $\Gamma = 1.00$). Recent measurements for $\Gamma = 1.00$ [25] yielded an exponent $\gamma_{\mathrm{eff}} = 0.321 \pm 0.002$, in essentially perfect agreement with the Grossmann–Lohse prediction but slightly larger than our $\Gamma = 0.50$ result.

Table 2. Results of least-squares fits of the power law equation (3) to the data in the classical regime.

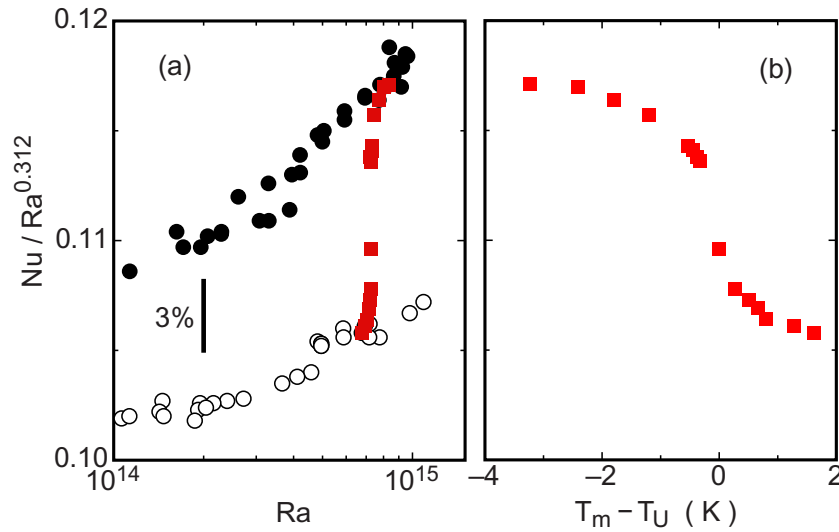| Data set	N_0	γ_{eff}
$T_{\text{m}} - T_{\text{U}} \lesssim -2\,\text{K}$	0.1040 ± 0.0011	0.3121 ± 0.0004
$T_{\text{m}} - T_{\text{U}} \lesssim -2\,\text{K}$	0.1044 ± 0.00002	0.312 (fixed)
$T_{\text{m}} - T_{\text{U}} \gtrsim 2\,\text{K}$	0.1020 ± 0.0037	0.3116 ± 0.0012
$T_{\text{m}} - T_{\text{U}} \gtrsim 2\,\text{K}$	0.1006 ± 0.00009	0.312 (fixed)

Figure 4. (a) The reduced Nusselt number $Nu/Ra^{0.312}$ on a linear scale as a function of Ra on a logarithmic scale. Solid (open) black circles: $T_{\text{m}} - T_{\text{U}} < -2\,\text{K}$ ($T_{\text{m}} - T_{\text{U}} > 2\,\text{K}$). Solid red squares: $Nu_{\text{red}} = Nu/Ra^{0.312}$ at nearly constant $\Delta T \simeq 10.3\,\text{K}$. (b) $Nu/Ra^{0.312}$ at nearly constant $\Delta T \simeq 10.3\,\text{K}$ as a function of $T_{\text{m}} - T_{\text{U}}$ on linear scales.

5.1.3. Transition to the ultimate state. In order to explore the dependence of the data on $T_{\text{m}} - T_{\text{U}}$ in more detail we show in figure 4(a) the results for the reduced Nusselt number $Nu_{\text{red}} = Nu/Ra^{0.312}$ on a linear scale as a function of Ra on a logarithmic scale. Here it becomes apparent that the $T_{\text{m}} - T_{\text{U}} < -2\,\text{K}$ data (solid circles) are higher than the $T_{\text{m}} - T_{\text{U}} > 2\,\text{K}$ data (open circles) by about 6% near $Ra = 10^{14}$ and about 10% near $Ra = 10^{15}$. In the classical regime $Ra \simeq 10^{13}$ (see figure 3 and table 2) the difference is 3.8%. In figure 4(a) we added a third set of data taken at nearly constant $\Delta T \simeq 10.3\,\text{K}$ but at various values of $T_{\text{m}} - T_{\text{U}}$. During these measurements T_{U} was not controlled and determined by the balance between the heat input to the Uboot from the HPCF-II and the cooling to the surrounding laboratory. It varied over the narrow range from 24.3 to 25.5 °C. The sample temperature T_{m} was controlled by feedback loops and was changed in small steps from 21 to 27 °C. Since T_{m} (and thus the fluid properties) changed, the data at constant ΔT led to a small variation of Ra. One sees that they cover the Nu_{red} range from the upper to the lower branch.
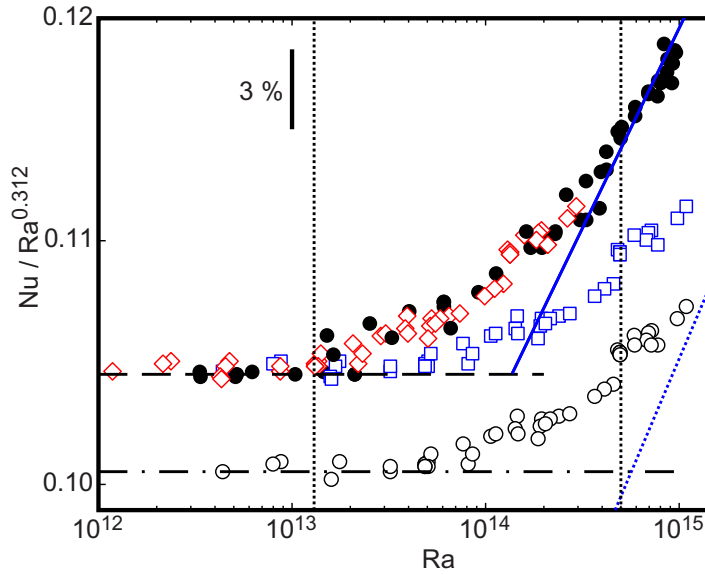
Figure 5. The reduced Nusselt number $Nu/Ra^{0.312}$ as a function of Ra for the 'closed' sample. Black solid circles: $T_m - T_U \lesssim -2\,\text{K}$. Black open circles: $T_m - T_U \gtrsim +2\,\text{K}$. Open squares (blue online): Nu values of the open black circles multiplied by 1.04. Open diamonds (red online): Ra values of the open squares divided by 3.7. The horizontal lines represent power laws for Nu with $\gamma_{\text{eff}} = 0.312$ and $N_0 = 0.1005$ and 0.1044. The solid (dotted) line (blue online) through (near) the data at the largest Ra corresponds to $\gamma_{\text{eff}} = 0.37$. The two vertical dotted lines represent our estimates of Ra_1^* and Ra_2^*.

The same constant ΔT results are shown also in figure 4(b), but as a function of $T_m - T_U$. Here one sees that the data become independent of $T_m - T_U$ when $|T_m - T_U| \gtrsim 2\,\text{K}$. This is the reason why the majority of data (the open and solid black circles) were taken as a function of Ra with $|T_m - T_U| \gtrsim 2\,\text{K}$.

In figure 5 we show all the data for the two states with $|T_m - T_U| \gtrsim 2\,\text{K}$ over the entire Ra range accessible in the experiment. One sees the classical state with $\gamma_{\text{eff}} = 0.312$ for $Ra \lesssim 10^{13}$. At larger Ra the two data sets trace out curves with remarkably similar shapes, albeit displaced both vertically and horizontally. To further explore the similarity between the two sets we multiplied the open circles by 1.04. This yielded the open blue squares, which now agree with the solid black circles in the classical range. Further dividing the Ra values of the open blue squares by 3.7 yielded the open red diamonds. One sees that these two transformations yielded agreement within the experimental scatter between the data at large and small $T_m - T_U$. This shows that the shapes of the curves traced out by the two data sets are the same.

Both data sets reveal a departure from the classical effective power law, with Nu increasing more rapidly with Ra than $Ra^{0.312}$ when $Ra > Ra_1^*$ where $Ra_1^* \simeq 1.5 \times 10^{13}$ for the solid circles and $\simeq 5 \times 10^{13}$ for the open circles. Henceforth we shall concentrate on the results for $T_m - T_U < -2\,\text{K}$. They continue to increase beyond the classical-state values, with an effective exponent that gradually becomes larger until $Ra_2^* \simeq 5 \times 10^{14}$ is reached. Beyond Ra_2^* one has $\gamma_{\text{eff}} \simeq 0.37 \pm 0.01$ as shown by the blue solid line in the figure. This result is consistent with the prediction of an asymptotic exponent $\gamma = 1/2$ modified by logarithmic corrections in the
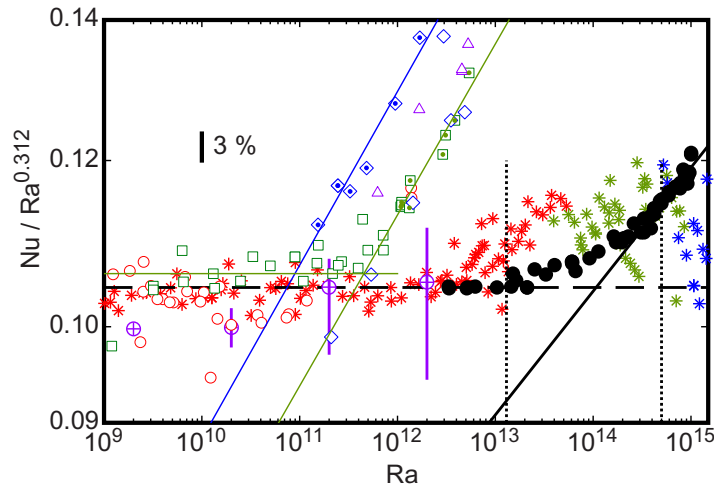
Figure 6. Comparison of the present results (solid black circles) with the Oregon (stars) [10], the Grenoble [12] (small open symbols), and the direct numerical simulation [79] (DNS) data. For the Oregon and Grenoble data we used different colors for different ranges of Pr. Red: $Pr < 1$. Green: $1 < Pr < 2$. Blue: $2 < Pr < 4$. Purple: $4 < Pr < 8$. The DNS data are for $Pr = 0.7$ and are shown as purple circles with plus signs and error bars. The slanting green and blue lines are power-law fits to the points with small dots in their centers.

ultimate state with turbulent BLs above the bottom and below the TP. The recent prediction by Grossmann and Lohse [65] for the form of the logarithmic corrections differs from that given by Kraichnan [5]; but our data cannot distinguish between these two theoretical results which both yield values of γ_{eff} which are roughly in the range from 0.38 to 0.40.

It is worth noting that the data in the transition range $Ra_1^* < Ra < Ra_2^*$ have significantly greater scatter than the data in the classical regime $Ra < Ra_1^*$ or those in the ultimate regime $Ra > Ra_2^*$. This indicates the existence of multiple states, presumably with subtly different BL configurations, during the complex transition from laminar to turbulent BLs.

We call attention to the fact that the transition range between the classical and the ultimate state can also be found, between about the same values of Ra_1^* and Ra_2^*, in results for the Reynolds number [25] and in measurements of vertical logarithmic temperature profiles that extend over much of the sample height [42].

5.2. Comparison with previous results

5.2.1. Comparison with the Grenoble, Oregon, and DNS data. Throughout this comparison we shall focus on our data for $T_{\text{m}} - T_{\text{U}} \lesssim -2\,\text{K}$; they will be shown as black solid circles in figures 6 and 8. We mention again that, for our results, Pr changed only over the narrow range from 0.79 near $Ra = 3 \times 10^{12}$ to 0.86 near $Ra = 10^{15}$. Throughout this comparison we shall show the data of others in red for $Pr < 1.0$, green for $1 < Pr < 2$, blue for $2 < Pr < 4$, and purple for $4 < Pr < 8$.

In figure 6 our measurements are compared with those of Niemela *et al* [10] (Oregon data) which are given as stars. For the large range $10^9 \lesssim Ra \lesssim 2 \times 10^{12}$ those results agree well with the power-law fit to our data in the classical regime which gave $Nu = 0.404 Ra^{0.312}$. One can

Table 3. Parameters obtained from power-law fits to various data sets. Ra_{min}, Ra_{max}, Pr_{min}, and Pr_{max} are the limits of the data sets used in the power-law fits. Nu_{red}^{cl} is the reduced Nusselt number $Nu/Ra^{0.312}$ used in the classical regime to determine the transition Rayleigh number Ra_t, which is taken to be the intercept with the power-law fit above Ra_t.

Sample	Grenoble [12]	Grenoble [12]	Flange [17]	Vintage [17]	Vintage [17]	Brass [14]	HPCF-IIe this work
$Ra_{min}/10^{11}$	1.5	10	20	20	8	2	5000
$Ra_{max}/10^{11}$	17	60	20	20	18	20	100 00
Pr_{min}	3.4	1.0	1.72	1.31	0.97	1.74	0.8
Pr_{max}	3.7	1.3	1.72	1.73	0.97	1.74	0.8
Nu_{red}^{cl}	0.106	0.106	0.098	0.096	0.094	0.104	0.104
γ^{eff}	0.395	0.382	0.371	0.399	0.404	0.396	0.37 ± 0.01
$Ra_t/10^{11}$	0.9	5	7	4	4	2	1100

argue that they rise above this power law as Ra approaches 10^{13}, perhaps signaling the beginning of a transition to the ultimate state, but in view of the scatter of the data this argument might not be convincing. It is noteworthy that the rise occurs when Pr is still less that one. However, as Ra increases beyond 10^{13}, no further increase above the classical power law occurs. It may be that this saturation is due to an increase of Pr, which begins to occur just in this Ra range and which is expected to shift Ra^* to higher values. In summary, the Oregon data show a departure from the classical power law near $Ra = 10^{13}$, but the evidence for having entered the ultimate state in our view remains inconclusive. We note that the original authors of this work believed that their data could be represented within their scatter and accuracy by a single power law with $\gamma_{eff} = 0.32$ over the entire Ra range up to 10^{17}, thus providing no evidence for an ultimate-state transition.

Also shown in figure 6, as small open symbols, are the Grenoble data [12] that fall in the range of the figure. One can see that they form distinct groups, depending on Pr. For $1 < Pr < 2$ (green symbols) there are data in the classical regime. They yield the effective exponent of 0.317 ± 0.003, which is consistent with $\gamma_{eff} = 0.312$ as adopted by us when possible systematic errors, particularly due to uncertainties in the side-wall corrections [73, 74], are taken into consideration. The actual values of $N_0 = Nu/Ra^{0.312}$ are also quite close to our result of 0.104. An average of the data for $10^9 < Ra < 10^{11}$ is only 2% higher, as shown by the horizontal green line in the figure.

For $1 < Pr < 2$ there is a sharp transition to a Ra range where the effective exponent is larger than the classical value of 0.312. In order to determine the Rayleigh number Ra_t at the transition and the effective exponent above it objectively, we selected a subset of points which we deemed to be above Ra_t and which seemed consistent with an effective power law. These points are indicated by a small dot in the open symbols. A power-law fit to these data and its intersection with the green horizontal line in the figure gave the parameters listed in table 3. For $2 < Pr < 4$ there also are sufficient data to warrant a power-law fit, but there are no classical-state data. We carried out the same analysis as for $1 < Pr < 2$, and used the result for the classical state for $1 < Pr < 2$ as the baseline to determine Ra_t. One sees from the table that the exponents are, within their statistical errors, consistent with 0.38, a value deemed typical
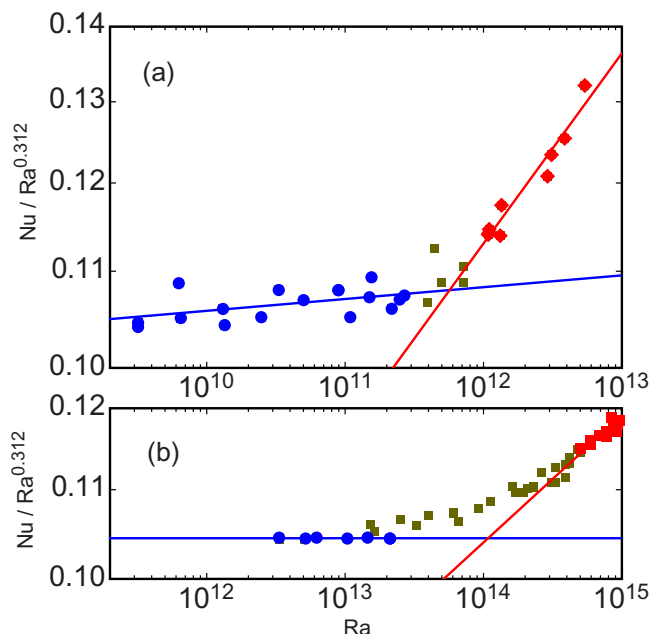
Figure 7. (a) A higher-resolution graph, on double logarithmic scales, of the Grenoble data [12] for $Pr = 1.1$ and 1.3. A power-law fit to the blue circles (red diamonds) yielded $\gamma_{eff} = 0.317 \pm 0.003$ ($\gamma_{eff} = 0.382 \pm 0.006$). The green squares were not used in either fit. (b) Our data are plotted with the same resolution as that used in (a), but with the horizontal axis shifted by two decades. A power-law fit to the blue circles (red diamonds) yielded $\gamma_{eff} = 0.3121 \pm 0.0004$ ($\gamma_{eff} = 0.371 \pm 0.01$). Our data show a transition region with a width of about 1.5 decades (green squares), whereas the Grenoble data suggest a sharp transition.

of the ultimate state. The values of Ra_t, however, in our view are too low to correspond to the shear-induced BL transition to turbulence that is expected to be characteristic of the ultimate-state transition. Further, as noted in [17], we see that the larger Pr value yielded a lower value of Ra_t, which is opposite to expectations for the BL shear instability. However, this trend is not confirmed by the data for the larger Pr range $4 < Pr < 8$ (purple open triangles), which do not have enough points to warrant an independent power-law fit but which are seen to fall between the other two data sets. Thus we must conclude that the Grenoble data do not establish an unambiguous trend of Ra_t with Pr. An explanation of the different values of Ra_t for the different data sets which seems likely to us are systematic errors of the equation of state or the transport properties near the critical point of helium that were used to calculate Ra and Nu; these errors could well change as the pressure and T_m (and thus Pr) are changed.

The Grenoble data for $Pr = 1.1$ and 1.3 are of sufficiently high precision and sufficiently detailed and plentiful to warrant a closer examination, as is done in figure 7(a). There they are compared with our results, which are shown in figure 7(b) on vertical and horizontal scales with the same resolution as in (a) but with the horizontal axis shifted by two decades. A remarkable difference between the two data sets is that the Grenoble data reveal a *sharp* transition suggestive of a continuous, or supercritical, bifurcation, whereas our data show a transition *range* of about 1.5 decades with indications of multi-stability in that range, which is inconsistent with

a continuous transition. We believe that a transition to a turbulent BL is unlikely to be sharp and continuous for at least two reasons. First, even for a uniform laminar BL the transition to turbulence does not occur at a unique value of the applied stress but rather will depend on the particular prevailing perturbations. In the time average this should lead to some rounding of the observed transition. Second, in the RB case the laminar BLs are not uniform. Rather, due to plume emission, they are highly fluctuating systems. In addition, they are non-uniform on longer length scales in the horizontal plane [38] when a LSC is present. Because of their spatial inhomogeneity they are unlikely to undergo a simultaneous transition from the laminar to the turbulent state at all lateral positions. These inhomogeneities are consistent with the existence of a transition *range*, as observed by us.

Finally, in figure 6, we show (as purple open circles with plusses and error bars) the results obtained from a direct numerical simulation by Stevens *et al* [79]. These data are for $Ra \leqslant 2 \times 10^{12}$. They do not show a transition for $Ra \leqslant 2 \times 10^{12}$ to a state with a larger effective exponent, and in that sense differ from the Grenoble data but agree with the Oregon data and with our results.

5.2.2. Comparison with the Chicago data. The 'Chicago' data are the earliest measurements of Nu at very large Ra. For $\Gamma = 0.5$ they were reported by Wu [78]. These results, after a correction[9] which shifted the data upward by an amount that varied smoothly from about 6% near $Ra = 10^9$ to about 10% near $Ra = 10^{14}$, are shown in figure 8(a) as open black circles. Their trend with Ra suggests $\gamma_{\text{eff}} \simeq 0.29$ [73]. However, they had not been corrected for the finite sample-wall conduction [73, 74]. That correction, based on Model 2 of [73], was applied in [73] and yielded the open purple squares in the figure. Those corrected data are consistent with $\gamma_{\text{eff}} = 0.312$, but the pre-factor N_0 of a power-law fit is about 10% lower than indicated by our results.

Just above $Ra = 10^{12}$ there is a discontinuity in the data, but this apparent 'transition' is not to a state with a larger γ_{eff}. We believe that this phenomenon is associated with a change of the place in the phase diagram near the critical point of helium where the data were taken, and that it is due to errors in the equation of state rather than a genuine change in the dependence of Nu on Ra. Thus we conclude that the Chicago data do not reveal any evidence of a transition to the ultimate state below their largest $Ra \simeq 3 \times 10^{14}$. Given the increase of Pr with Ra for these data and the expected dependence of Ra^* on Pr, we find that the absence of a transition to the ultimate state in these data is consistent with the Oregon data and with our results.

5.2.3. Comparison with data from Roche et al. Finally, in figures 8(b)–(e), we display several data sets obtained in different sample cells, all with $\Gamma = 0.5$, by Roche *et al* [14, 17]. Many of them show a transition at Ra_{t} from the classical state to a state with a larger γ_{eff}. Whenever there are adequate classical-state data, these sets are consistent with the exponent 0.312, but the pre-factor of the corresponding power law varied between different sets and generally was somewhat lower than our result $N_0 = 0.104$. We analyzed the sets with sufficient data both above and below Ra_{t} as described above for the Grenoble data. The results are given in table 3. The effective exponent varies from 0.371 to 0.404. A reason for this variation is not obvious to us. The value of Ra_{t} varied significantly as well, from 0.9×10^{11} to 7×10^{11}, again for non-obvious reasons.

---

[9] The data of Wu [78] were re-evaluated on the basis of new fluid properties by Niemela *et al* [80].
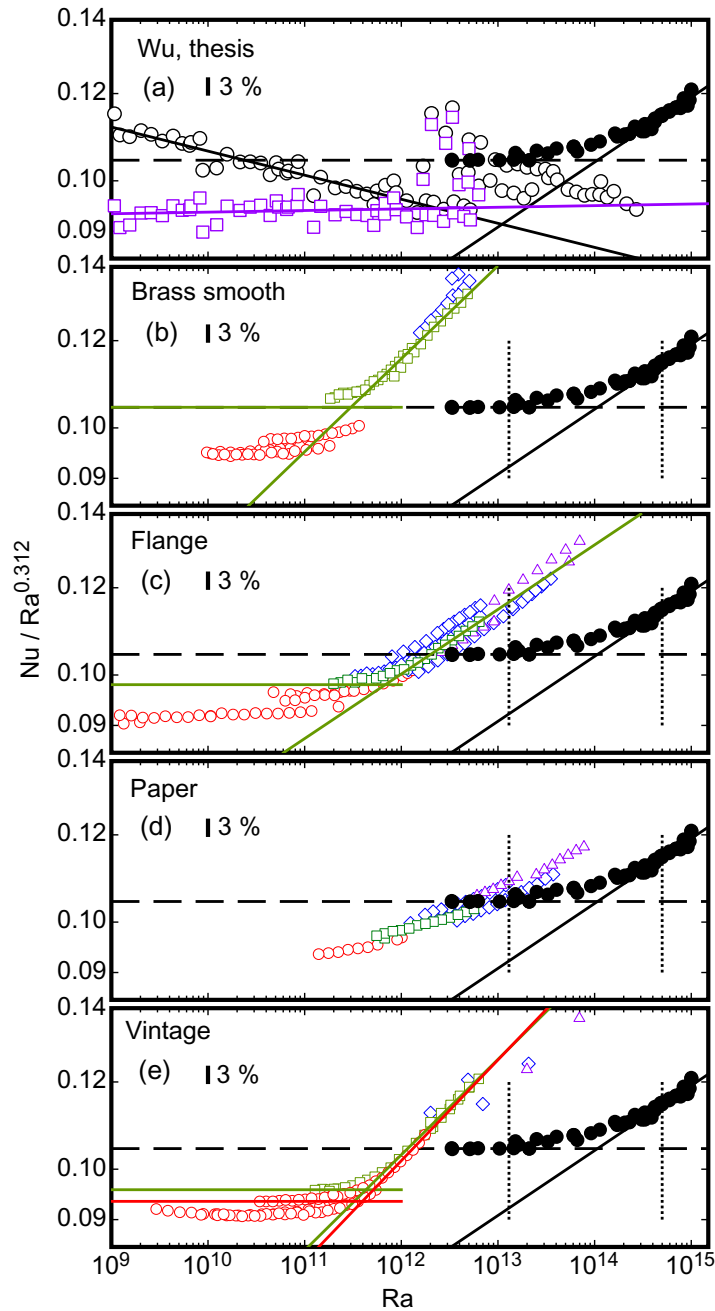
Figure 8. Comparison of the present results (solid black circles) with (a) the Chicago data [78], (b) data from [14], and (c)–(e) data from [17]. We used different symbols for different ranges of Pr. Red open circles: $Pr < 1$. Green open squares: $1 < Pr < 2$. Blue open diamonds: $2 < Pr < 4$. Purple open triangles: $4 < Pr < 8$. The horizontal black dashed line is our best estimate for the classical state. The other lines are fits described in the text. In (a) the open circles (purple open squares) are data without (with) a correction for the conductance by the side wall.

Figure 9. The transition Rayleigh number Ra_t as a function of Pr. The data are from table 3. Blue diamond: HPCF-IIe. Red circles: the remaining points in the table. The solid line is a fit of the theoretically expected dependence $Ra_t \propto Pr^{1.65}$ (equation (5)) to the HPCF-IIe point.

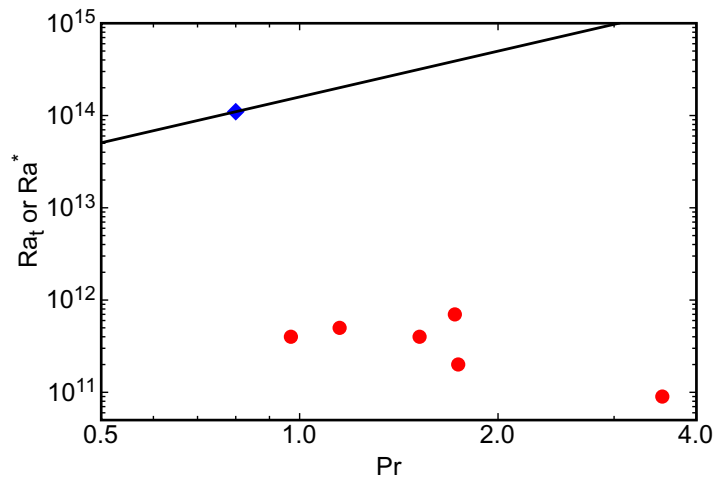In figure 9 we show Ra_t as a function or Pr as red solid circles. A trend with Pr is, in our view, not firmly established, although the point at the largest Pr suggests a decrease with increasing Pr. Such a decrease would be contrary to the theoretical expectation for a shear-driven BL transition to turbulence [36]. The theoretically expected result is obtained by assuming that the transition to the ultimate state occurs at a Rayleigh number Ra^* at which the bulk Reynolds number (and thus also the shear Reynolds number $Re_s^* \propto \sqrt{Re^*}$)) attains a certain constant value Re^*. Taking $Re \propto Ra^{0.423}/Pr^{0.70}$, one finds

$$Ra^* = 1.6 \times 10^{14} Pr^{1.65}. \tag{5}$$

Here the constant coefficient was adjusted so that the relation passes through the point $Ra^* = 1.1 \times 10^{14}$ for $Pr = 0.8$ shown as the blue diamond in the figure, which is the result from this work. The line through that point corresponds to equation (5). One sees that the red circles do not reproduce the predicted increase of Ra^* with Pr, as already noted by Roche *et al* [17]. However, we do not find convincing evidence in these data that larger values of Pr *favor* the transition to the state with the larger exponent.

5.3. Open sample

As discussed in section 4, initially (for HPCF-I, IIa, and IIb) gaps with an average width of about 1 mm were left between the top and bottom plates and the side wall in order to permit the SF$_6$ to pass from the Uboot into the sample. These samples are referred to as the 'open' samples. Although the gap widths were negligible compared to the sample dimensions, it was appreciated later that they could significantly modify the system, depending on the temperature difference $T_m - T_U$ between the sample (T_m) and the Uboot (T_U). When $T_m < T_U$ ($T_m > T_U$), then the sample density is larger (smaller) than the density of the fluid in the Uboot. In the presence of gravity this density difference will lead to flow through the gaps, in the upward (downward) direction when $T_m - T_U > 0$ (< 0). In the presence of such externally imposed flows the system
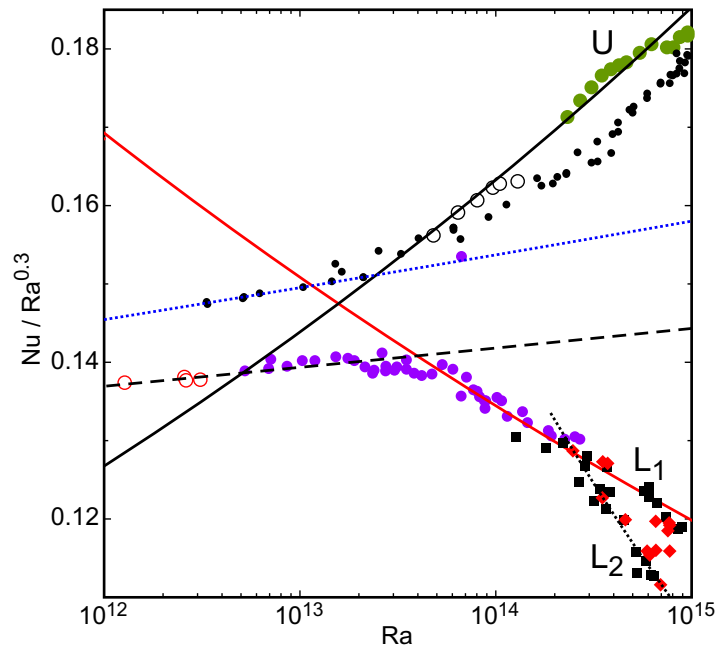
Figure 10. The reduced Nusselt number $Nu/Ra^{0.3}$ as a function of the Rayleigh number Ra on a logarithmic scale. The purple solid circles, black solid squares, and red solid diamonds are from HPCF-I, HPCF-IIa, and HPCF-IIb respectively, using SF_6 at various pressures. The open red circles are from HPCF-I using N_2. All of those data were shown before in [23]. The open black and solid green circles are new data from HPCF-IIb using SF_6 at 12.2 bar ($Pr = 0.823$) and 18.8 bar ($Pr = 0.863$) respectively. The small black dots are our results for HPCF-IIe (the closed sample). The lines correspond to power laws $Nu = N_0 Ra^{\gamma_{eff}}$ with $N_0 = 0.111$, $\gamma_{eff} = 0.308$ (dashed black line), $N_0 = 0.674$, $\gamma_{eff} = 0.25$ (red solid line), $N_0 = 12.3$, $\gamma_{eff} = 0.16$ (black dotted line), $N_0 = 0.0277$, $\gamma_{eff} = 0.36$ (black solid line), and $N_0 = 0.104$, $\gamma_{eff} = 0.312$ (dotted blue line). The labels U, L_1, and L_2 identify the 'upper branch', 'lower branch 1', and 'lower branch 2'.

can no longer be regarded as a genuine RBC. Instead, it has features in common with examples of indoor ventilation problems that have been discussed, for instance, by Linden [81].

Previously [23, 52, 75] we presented some measurements of Nu for the open system. These measurements were made with $T_m = 25\,°C$. During those early stages of this investigation T_U was not actually measured, but more recent experience suggests that it was between 23 and $24\,°C$. Thus the data are for $T_m - T_U > 0$. The results are shown again in figure 10 in the form of $Nu/Ra^{0.3}$ as a function of Ra. The purple solid circles, black solid squares, and red solid diamonds are from HPCF-I, HPCF-IIa, and HPCF-IIb respectively and were obtained with SF_6. The open red circles were measured using nitrogen in HPCF-I. For comparison the closed-sample data are shown as small black dots, with the power-law fit in the classical range (see figure 3) with $\gamma_{eff} = 0.312$ shown as a dotted blue line. For $Ra \lesssim 4 \times 10^{13}$ the open-sample data are described well by a power law with $\gamma_{eff} = 0.308$ (the dashed black line), reasonably

consistent with the classical state; however, they are somewhat lower than the closed-sample data.

With increasing Ra the measurements from HPCF-I (purple solid circles in figure 10) revealed a transition to a new state beyond $Ra_{t1} \simeq 4 \times 10^{13}$. Within our resolution Nu was continuous at that transition, and the transition was sharp. In those respects the transition differed from the ultimate-state transition seen for the closed sample but was similar to the transitions at $Ra_t = \mathcal{O}(10^{11})$ found by Chavanne *et al* [12] (see figures 6 and 7(a)) and Roche *et al* [17]. However, the present case is very different from the previous ones in that γ_{eff} decreased whereas for the prior work it increases. Above Ra_{t1} the data could be described well by a power law with $\gamma_{eff} = 0.25$, as shown by the solid red line in the figure. We shall refer to this state as the 'L$_1$' state or branch.

In a recent paper [65] Grossmann and Lohse pointed out that, with increasing Ra, the transition away from the classical state can take several possible forms. Whereas previously [5, 6] the ultimate-state transition was assumed to involve a simultaneous shear-induced transition to turbulence in both the viscous and the thermal BL, this need not be the actual sequence of events. They proposed three possibilities that may prevail when the viscous BL becomes turbulent. One of these is that the thermal BL remains laminar (i.e. of the Prandtl–Blasius type in the time average) and that the heat transport is background dominated (see section 3.2 of [65]). For that case they derived $Nu \sim Ra^{1/5}$, with logarithmic corrections which yield $\gamma_{eff} \simeq 0.22$–0.23. Within experimental and theoretical uncertainties this is consistent with our result $\gamma_{eff} \simeq 0.25$ for the L$_1$ branch.

Further measurements, with HPCF-IIa (black solid squares in figure 10) and HPCF-IIb (red solid diamonds in figure 10), revealed the existence of yet another branch, which we labeled as L$_2$. The transition to this branch occurred at $Ra_{t2} \simeq 2.5 \times 10^{14}$. The new branch co-existed with L$_1$. The precise conditions that determined which branch was chosen by the system were not explored in detail, but they involved $T_m - T_U$ and thus the strength of the presumed external current entering or leaving the sample. A power-law fit to the L$_2$ data yielded $\gamma_{eff} \simeq 0.16$. This result is consistent with the theoretical value (see section 3.1 of [65]) $\gamma = 1/8$ which logarithmic corrections for a state with a turbulent viscous BL and a laminar thermal BL, with the heat transport dominated by the emission of plumes. For this state the logarithms modify γ so that $\gamma_{eff} \simeq 0.14$, not very different from the experimental value.

When it was realized that $T_m - T_U$ played an important role in the choice of the state of the system, new measurements were made with HPCF-IIb and with $T_m - T_U \lesssim -2\,\mathrm{K}$. Those data are shown as open black and solid green circles in figure 10. They fall somewhat above the closed-sample data (small black dots), but seem reasonably consistent with a perhaps slightly modified transition to the ultimate state. This upper branch is labeled 'U'. A power-law fit to these data yielded $\gamma_{eff} = 0.36$ and is represented by the solid black line in the figure.

5.4. Half-open sample

As a first attempt to prevent the external currents through the sample due to the difference between T_m and T_U, we sealed the bottom plate to the side wall but left the gap between the TP and the side wall so that the gas could still enter the sample. We refer to this case, which is HPCF-IIc, as the half-open sample. The results for Nu are shown in figure 11 as solid red squares for $T_m - T_U < -2\,\mathrm{K}$ and as open red squares for $T_m - T_U > 2\,\mathrm{K}$. As might be expected, the data for $T_m - T_U < -2\,\mathrm{K}$ agree well with the results from the closed sample (small solid
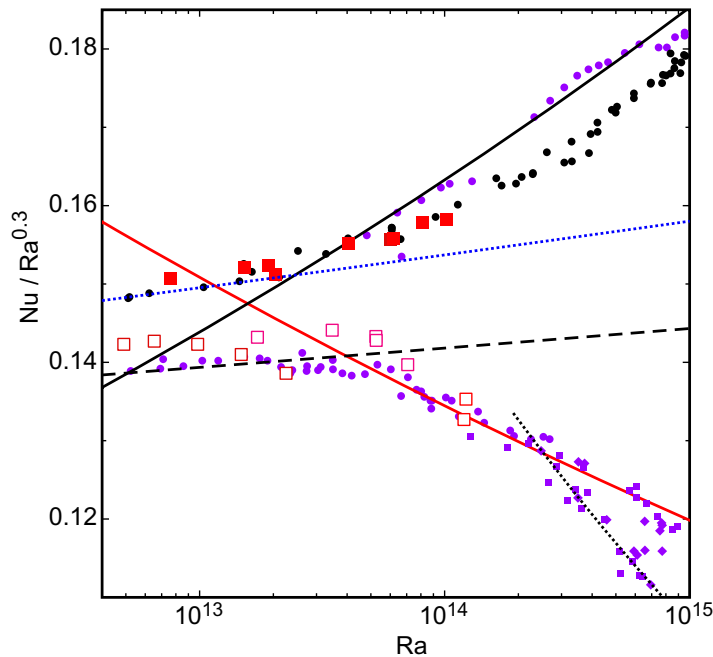
Figure 11. The reduced Nusselt number $Nu/Ra^{0.3}$ as a function of the Rayleigh number Ra on a logarithmic scale. Small purple symbols: open sample (see figure 10). Small black circles: closed sample, $T_m - T_U < -2\,$K (see figure 5). The larger red symbols are for the half-open sample. Solid squares: $T_m - T_U < -2\,$K. Open squares: $T_m - T_U > 2\,$K.

black dots). This is so because the relatively dense gas, which in the open sample escapes through the gap at the bottom plate, cannot do so in this case. However, the case where the sample gas is less dense than the gas in the Uboot ($T_m - T_U > 2\,$K, open squares) seems to be influenced by external currents near the TP and the corresponding data are close to those for the open sample (purple solid circles). Indeed they even reveal the transition at Ra_{t1} to the L_1 state.

6. Summary

In this paper we reported results for the Nusselt number Nu over the range of the Rayleigh number Ra from 3×10^{12} to 10^{15}. Data were presented for three different sample cells, all of cylindrical shape and of aspect ratio $\Gamma = 0.50$. The cells, known as the High-Pressure Convection Facilities (HPCFs), were located in a pressure vessel referred to as the 'Uboot' of Göttingen. The Uboot and the HPCF were filled with the gas sulfur hexafluoride (SF_6) at various pressures up to 19 bar. This fluid had a Prandtl number Pr which varied over the narrow range from 0.79 to 0.86 as the pressure (and thus Ra) changed from its smallest to its largest value.

One of the samples was completely sealed. In that case a 2.5 cm diameter tube penetrated the side wall at mid height and allowed the SF_6 to enter the HPCF from the Uboot; that tube was then closed off by a remotely operated valve after an equilibration time of several hours and before measurements were made. This version of the HPCF is known as the 'closed' sample. Another version was allowed to have a small gap, of width approximately equal to

1 mm, between the side wall and the top and bottom plate to allow the sample gas to enter the HPCF. This version is known as the 'open' sample. A third version, known as the 'half-open' sample, had the side wall sealed to the bottom plate while the gap was allowed to persist at the TP.

It turned out that the three samples produced qualitatively different dependences of Nu on Ra. Only the closed sample can be regarded as corresponding well to the idealized closed-system Rayleigh–Bénard problem. For the open and half-open samples gas currents were able to enter and leave the sample through the gaps at the plates, driven by the small density differences that existed between the sample fluid at a mean temperature T_m and the fluid in the Uboot at a temperature T_U. The results for $Nu(Ra)$ were then qualitatively different depending on whether T_m was larger or smaller than T_U. Nonetheless the open and half-open samples produced interesting effects. Under certain conditions there was a sharp but continuous transition from a state below $Ra_t \simeq 4 \times 10^{13}$ where $Nu \sim Ra^{\gamma_{eff}}$ with $\gamma_{eff} \simeq 0.31$ to a state above it with $\gamma_{eff} \simeq 0.25$. Another state with $\gamma_{eff} \simeq 0.16$ was found as well. Possible explanations of these findings in terms of different laminar or turbulent conditions in the thermal and viscous BLs adjacent to the top and bottom plates were offered by Grossmann and Lohse [65]. We refer the reader to sections 5.3 and 5.4 as well as to [65] for a more detailed discussion of these interesting phenomena.

The primary focus of this paper has been on the closed sample. Even for this case the results for $Nu(Ra)$ depended somewhat on $T_m - T_U$, but in contradistinction to the open and half-open samples the dependence was simply a shift of the curve without any change in shape. This dependence persisted in spite of the extensive shielding of the sample that was provided, and we do not know its origin. However, for $Ra \lesssim 10^{13}$ we found that the effective exponent of Nu was 0.312 ± 0.002, regardless of T_m and T_U. This exponent value is consistent with, but more accurate than, many other measurements at smaller Ra. It also agrees quite well with the value 0.323, which follows from a power-law fit to data generated from the Grossmann–Lohse model [50] for $Pr \simeq 0.8$ (albeit for $\Gamma = 1.00$) in the range $10^{12} \lesssim Ra \lesssim 10^{13}$. We note that very recent measurements [22] for $\Gamma = 1.00$ yielded an exponent of 0.321 ± 0.002, in near-perfect agreement with the Grossmann–Lohse value but slightly larger than our result for $\Gamma = 0.50$. Thus we believe that the state of the system with $Ra \lesssim 10^{13}$ is the classical state of RBC with laminar BLs below the top and above the bottom plate.

In the range $Ra_1^* \leqslant Ra \leqslant Ra_2^*$, with $Ra_1^* \simeq 1.5 \times 10^{13}$ and $Ra_2^* \simeq 5 \times 10^{14}$, the system gradually underwent a transition and γ_{eff} increased from 0.32 to 0.37 as Ra changed by about one and a half decades. We believe that this phenomenon reflects the transition to the ultimate state predicted by Kraichnan [5] and re-examined recently by Grossmann and Lohse [65]. In the ultimate state, which we found for $Ra > Ra_2^*$, the effective exponent was 0.37 ± 0.01. This is reasonably consistent with the predicted asymptotic exponent $\gamma = 1/2$ and the expected logarithmic corrections [65]. Our conclusion that the state above Ra_2^* is the ultimate state is supported by the transitions and exponent-values found in simultaneous measurements of the Reynolds number Re [25] (a detailed discussion of those results is beyond the scope of this paper). Evidence for the transition range, with about the same values of $Ra_{1,2}^*$, can be found also in recent measurements of logarithmic vertical temperature profiles that extend throughout most of the sample [42].

It is worth emphasizing that the transition from the classical to the ultimate state is *not* a continuous transition where $Nu(Ra)$ is continuous but its effective exponent changes discontinuously, such as was found at $Ra_t \simeq 4 \times 10^{13}$ in the open sample (see figure 10) as well

as in the work of [12] (see figures 6 and 7). Instead there was a transition *range* spanning a factor of 30 or so in Ra over which the transition occurred. In this transition range the results for $Nu(Ra)$ scattered more than below or above it and were often irreproducible at the level of our resolution from one point to another, suggesting the existence of many states which differed in detail.

The observed transition range (as opposed to a unique value of Ra^*) is not surprising for two reasons. First, transitions involving shear-flow instabilities are known to depend on the size of prevailing local perturbations and thus will occur at different values of the Re (or in our case Ra) number. In addition, in the present case the basic state, i.e. classical RBC, is known to have laminar BLs which are non-uniform in the horizontal plane [38]. Since the BLs and the shear applied to them by the turbulent bulk are known to be spatially inhomogeneous, one should not expect a sharp transition.

In this paper we also provide a re-examination of earlier measurements. Some of these indicated a transitions to a state where γ_{eff} assumes a value near 0.38, but the transitions occurred at the rather low values of Ra_{t} between 10^{11} and 10^{12}. All of these data involved a range of Pr. We separated them into subsets corresponding to a unique value, or spanning only a small range, of Pr. Within each subset one sees that the scatter of these data is much less than it is when all Pr values are considered jointly. Some of the subsets reveal a well defined transition. These transitions differ qualitatively from the one observed by us in that they are sharp and continuous, without any resolved transition range. Estimates of the shear Reynolds number for them are in the range near 100 or less, which to us seems too low for a turbulent BL shear transition. Based on our measurements of Re, and on recent calculations by DNS of the shear Reynolds number Re_{s} [82], as well as on earlier estimates [36], indicate that the BL shear transition at Ra^* to the ultimate state should not occur until $Ra = \mathcal{O}(10^{14})$ is reached. Thus, in our view, the transitions observed near $Ra = 10^{11}$–10^{12} are unrelated to the ultimate-state transition, but we cannot offer an alternative explanation for their existence.

This paper concludes with a number of appendices which examine the possible effect of several experimental factors on our results. None of them is found to have a significant influence.

Appendix A. Effect of tilting the sample

All data for this study were taken with HPCF-IIe (the closed sample). Measurements were made with a leveled sample (a tilt angle $\beta < 0.1$ mrad, runs 100918–110102), and with the same sample tilted relative to gravity. The tilt was used to localize the azimuthal orientation of the LSC plane. Based on measurements with smaller samples of aspect ratio $\Gamma = 1.00$ [31] and
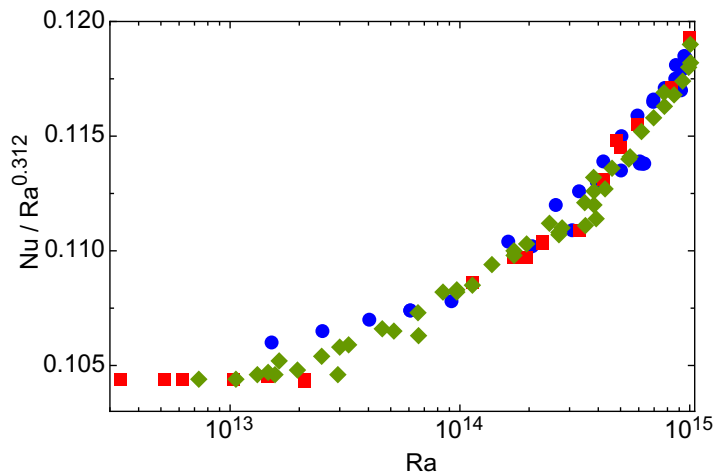
Figure A.1. The reduced Nusselt number $Nu/Ra^{0.312}$ as a function of the Rayleigh number Ra for $T_{\mathrm{m}} - T_{\mathrm{U}} < -2\,\mathrm{K}$ as a function of the Rayleigh number for three different tilt angles β of the sample relative to gravity. Blue circles: 'level', $\beta < 10^{-4}\,\mathrm{rad}$. Green diamonds: $\beta \simeq 0.003\,\mathrm{rad}$. Red squares: $\beta \simeq 0.014\,\mathrm{rad}$.

0.50 [83], both with $Pr \simeq 4$, we do not expect a measurable influence of the tilt on the heat transport for our case of $\Gamma = 0.50$ and $Pr \simeq 0.8$. This is indeed borne out by the data.

In one case the tilt angle was $\beta = 3\,\mathrm{mrad}$ (runs 110115–110610). The tilt direction was at an angle $\theta_\beta = 3\pi/2\,\mathrm{rad}$ relative to the azimuthal origin of the sidewall thermometers that were used to monitor any LSC. In the other case we had $\beta = 14\,\mathrm{mrad}$ and $\theta_\beta = 0.0\,\mathrm{rad}$ (runs 110618–110919). The results for the Nusselt number for the data with $T_{\mathrm{m}} - T_{\mathrm{U}} < -2\,\mathrm{K}$ are shown in figure A.1 as blue circles (no tilt), green diamonds ($\beta = 3\,\mathrm{mrad}$) and red squares ($\beta = 14\,\mathrm{mrad}$). There is no significant difference between the three data sets, showing that the effect of the tilt on Nu is well below 1 per cent.

Appendix B. Non-Boussinesq effects

Non-Oberbeck–Boussinesq NOB effects [32, 33] on Nu in a gas have been studied quantitatively using ethane gas as the fluid [84, 85]. Although variations of all fluid properties contribute in principle, for gases the primary contribution comes from the temperature dependence of the density and can be described approximately by the parameter $\alpha\Delta T$ (see figure 4 of [84]). All our measurements were made with $\Delta T \lesssim 21\,\mathrm{K}$ where we expect the NOB effects to be small. For a perfect gas one has $\alpha\Delta T = \Delta T/T$ with T in K, which for $\Delta T \simeq 20\,\mathrm{K}$ and at a mean temperature of 21 °C or 294 K is close to 0.07. However, the properties of SF_6 in our pressure range up to 19 bar show large deviations from those of a perfect gas. Figure B.1(a) shows $\alpha\Delta T$ as a function of Ra for the data with $T_{\mathrm{m}} - T_{\mathrm{U}} < -2\,\mathrm{K}$. The different-colored circles are, from left to right, for different isobars with pressures of approximately 4, 5, 8, 12, 15, and 19 bar. For the points shown as red squares we had $19 < \Delta T < 21\,\mathrm{K}$, which were the largest temperature differences employed in this work. The dotted line is the approximate perfect gas result. One sees that $\alpha\Delta T$ was mostly below 0.1 and always below 0.14.
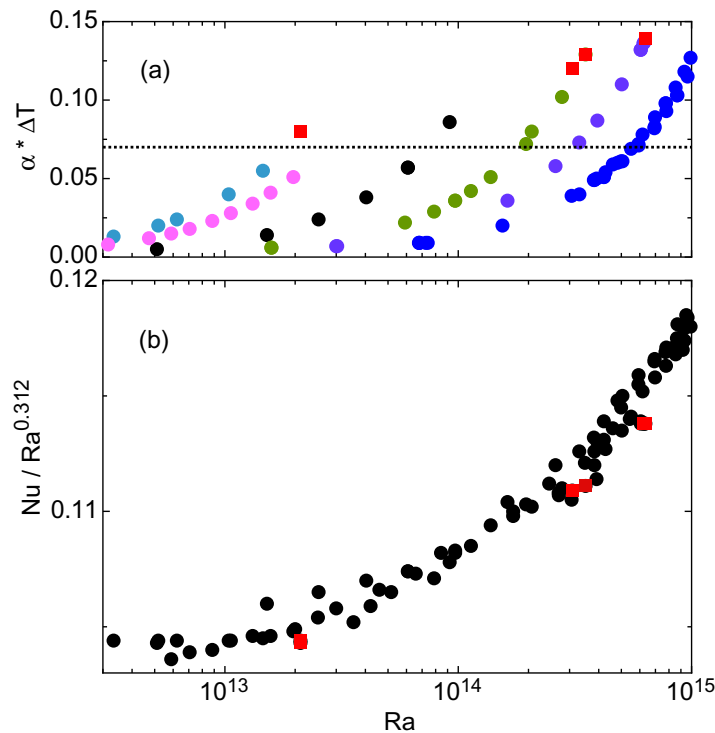
Figure B.1. (a) The parameter $\alpha \Delta T$ as a function of Ra. The circles of various colors are, from left to right, for approximately 4, 5, 8, 12, 15, and 19 bar. The red squares are points for which $19 < \Delta T < 21$ K. The dotted horizontal line indicates the perfect-gas value 0.071 for $\Delta T = 21.0$ K and $T_{\mathrm{m}} = 294.2$ K. (b) The reduced Nusselt number for $T_{\mathrm{m}} - T_{\mathrm{U}} < -2$ K as a function of the Rayleigh number. Black circles: $\Delta T < 19$ K. The red squares are points for which $19 < \Delta T < 21$ K and correspond to the red squares in (a).

In figure B.1(b) we show the reduced Nusselt number for the data with $T_{\mathrm{m}} - T_{\mathrm{U}} < -2$ K. All data are shown as solid black circles, except for the ones with $19 < \Delta T < 21$ K which are given as red squares. One sees that the points with large ΔT are systematically lower than the remaining results, but only by about 1.4% at the highest pressure where $\alpha \Delta T$ is largest and by about 0.7% at the lowest pressure where $\alpha \Delta T$ is about a factor of two smaller. It is surprising that NOB effects *reduce Nu* in the present case because in the case of ethane [84, 85] they *enhanced Nu*, albeit only by a small amount. A reduction of Nu due to NOB effects was observed, however, in the case of a liquid, namely water [86], but again only by a per cent or so for $\Delta T \simeq 20$ K. In any case, what matters for this work is that NOB effects are negligible for nearly all of our data.

Appendix C. The parameter ξ of Niemela and Sreenivasan

Recently Niemela and Sreenivasan [34] introduced the parameter

$$\xi = \frac{\eta}{\lambda} \frac{\Delta \lambda}{\Delta \eta}, \tag{C.1}$$

Figure C.1. The parameter ξ introduced by Niemela and Sreenivasan [34] (see text). The data are for the following approximate pressures: blue diamonds: 4 bar; red diamonds: 5 bar; green circles: 8 bar; green triangles: 10 bar; red squares: 12 bar; red triangles: 14 bar; yellow circles: 15 bar; green squares: 16 bar; black circles: 18 and 19 bar.

where λ is the fluid conductivity, η is the shear viscosity and Δ indicates the difference of the value of the prop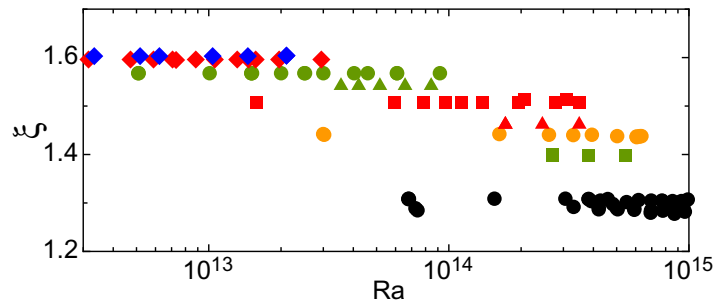erty following it at the bottom and at the top of the sample. Thus, ξ is a measure of the relative sizes of the contributions to the NOB conditions from λ and η. The authors state that their data for a cell with $\Gamma = 1.0$ [19, 34] and $\Gamma = 4.0$ [20] make a transition from a state of lower to one of higher Nu as ξ changes in their experiments from positive values of order 1 to negative values of -1 or less, both states having a common scaling exponent with a value slightly above 0.3. The authors assert that the transition between the two states, where roughly $Nu \sim Ra^{0.5}$, should not be interpreted as the ultimate state; rather, the data correlate well with the material parameter ξ.

The values of ξ for our data are plotted in figure C.1. We see that at a given pressure ξ is essentially independent of Ra, and thus of ΔT. The value of ξ depends slightly upon the pressure, varying over the range $1.6 \gtrsim \xi \gtrsim 1.3$ as the pressure changes from about 4 to about 19 bar. Thus, for all of our data ξ remains positive and slightly above 1 and the transition seen in the data of [19, 20, 34], which were taken near the critical point of helium, is not expected to occur in our fluid-property range.

Appendix D. Effect of horizontal temperature variations in the top and bottom plate

Maintaining the top and bottom plates at a uniform temperature, even in the presence of the large vertical heat currents up to 1 kW or so, is a significant experimental challenge, especially when the plates become very large as in our experiment where the diameter was well over a meter and the mass of the plates was of order 200 kg.

Our TP was cooled by water passing through a pair of double spiral channels [23]. The two members of the pair were in parallel, and each pair consisted of anti-parallel (i.e. an inward and an outward flowing) spirals. The distance between the centers of adjacent channels was 2.54 cm, and the channels had a depth $d = 1.26$ and a width $w = 1.27$ cm (cross sectional area of 1.60 cm^2). These dimensions were kept small to minimize lateral temperature variations on small length scales of the order of the plate thickness. However, as will be seen below, the small channel cross section did lead to a significant flow resistance, and a somewhat larger channel
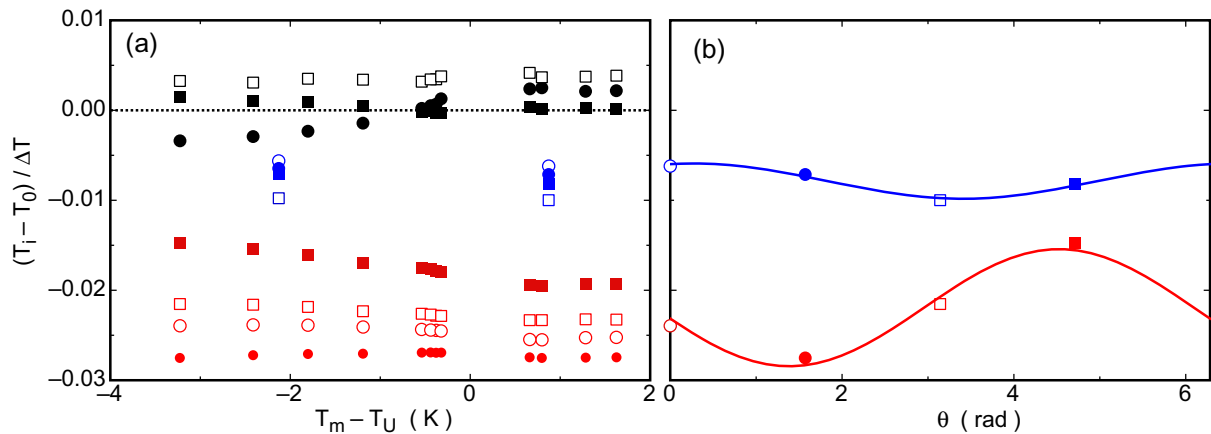
Figure D.1. (a) The normalized radial temperature variation $(T_i - T_0)/\Delta T$ as a function of the temperature difference $T_m - T_U$ between the mean sample temperature and the Uboot temperature (for details, see text). Red symbols: TP data for the weaker water circulation driven by a Nelab RTE7 circulator. Blue symbols: data for the TP with the stronger water circulation driven by a Wilo pump. Black symbols: data for the top member of the bottom-plate composite. Open circles, solid circles, open squares, and solid squares are for $T_0 - T_i$ with $i = 1, 2, 3$, and 4 respectively. (b) The azimuthal temperature variation for two examples. The solid lines are a fit of a sine function with an adjustable phase and amplitude to the data.

cross section might have been optimal. There is a constraint on the channel depth provided by the plate thickness; a much greater thickness would lead to excessive weight and cost of the plate.

The plate temperatures were determined by five thermometers in both the TP (between the water channels) and the top of the bottom-plate composite [52]. All ten thermometers were placed in small holes in the plates, with their tips within 1 mm or so of the copper–fluid interface. One thermometer (T_0) was located at the plate center. The other four T_i, $i = 1, \ldots, 4$, were equally spaced azimuthally at angular intervals of $\pi/2$ rad and were positioned radially at a distance of $0.42D$ from the center. The plate temperatures T_b and T_t used to calculate ΔT (and thus Nu and Ra) were the averages of the five readings in a given plate.

Here we report on the results obtained with HPCF-IIe. Initially (runs 110918–110410) the water flow was generated directly by a Neslab RTE7 circulator capable of generating a pump head corresponding to approximately 0.5 bar, which yielded a relatively small flow rate near $15\,\text{cm}^3\,\text{s}^{-1}$ ($0.05\,\text{m}^3\,\text{h}^{-1}$) in each of the two double spirals, corresponding to a mean velocity v of about $10\,\text{cm}\,\text{s}^{-1}$ or a Reynolds number $Re = vd/\nu = \mathcal{O}(10^3)$. Judged by the value of Re, the flow probably was laminar. In figure D.1(a) we show $(T_i - T_0)/\Delta T$, $i = 1, \ldots, 4$ as a function of $T_m - T_U$ as red symbols. Those data were taken at a pressure of 18.8 bar and with $\Delta T \simeq 10\,\text{K}$ (run 110311–110326) corresponding to $Ra \simeq 8 \times 10^{14}$, but similar measurements over a range of ΔT and at other pressures gave similar results. The dependence on $T_m - T_U$ is weak. The azimuthally averaged radial temperature variation $(\langle T_i \rangle_{i=1,\ldots,4} - T_0)/\Delta T$ is a little over 2%, which was judged larger than desirable. The azimuthal variation of $(T_i - T_0)/\Delta T$ for
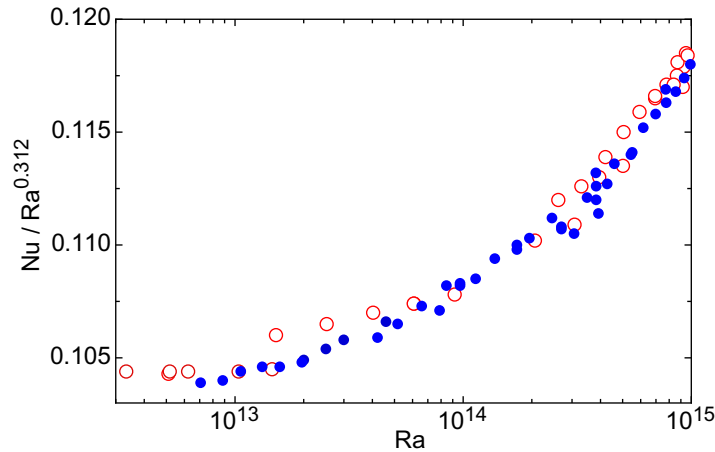
IOP Institute of Physics Φ DEUTSCHE PHYSIKALISCHE GESELLSCHAFT

Figure D.2. The reduced Nusselt number as a function of the Rayleigh number for $T_m - T_U < -2\,\mathrm{K}$. Open red (solid blue) circles: data taken with low (high) water flow rate in the TP cooling channel.

$T_m - T_U = -3.2\,\mathrm{K}$ (run 110311) is shown in figure D.1(b) as red symbols. It can be fitted well by a sine curve, suggesting that its origin is the LSC in the bulk fluid [28, 87, 88].

In order to increase the flow rate of the water in the top plate, we modified the top-plate water cooling circuit (starting with run 110426). We drove a primary circuit by a Wilo model MHI 205-1 pump, which could generate a pressure differential across the top-plate water channel of 4.2 bar and yielded a flow rate $170\,\mathrm{cm^3\,s^{-1}}$ ($0.6\,\mathrm{m^3\,h^{-1}}$) in each double spiral, corresponding to a mean flow velocity $v \simeq 100\,\mathrm{cm\,s^{-1}}$ or $Re = \mathcal{O}(10^4)$. This flow almost certainly was turbulent. The primary water circuit was thermally coupled by a heat exchanger to a secondary cooling circuit driven and temperature-controlled by the Neslab RTE7 circulator. This circulator was servoed so as to maintain T_t at its desired value. The results for $(T_i - T_0)/\Delta T$ are shown in figure D.1(a) as blue symbols and for two values of $T_m - T_U$. There was a significant improvement, with $(\langle T_i \rangle_{i=1,\dots,4} - T_0)/\Delta T$ as small as 0.8%. The remaining azimuthal variation for $T_m - T_U = -2.2\,\mathrm{K}$ is shown as blue symbols in figure D.1(b).

In order to judge whether one or the other of the top-plate cooling circuits is adequate to yield valid results for Nu, we show in figure D.2 results for $Nu(Ra)$ obtained by the first method as red open circles. Data obtained with the improved top-plate cooling method are represented by the solid blue circles. The two sets agree with each other very well and essentially within their scatter, indicating that there is no systematic dependence on the cooling method and that either method was indeed adequate for Nusselt number measurements.

The bottom plate was a composite of two copper plates with a thin Lexan layer between them. The heat current passing through this composite was generated by Joule heating with a heater wire imbedded in grooves milled into the underside of the bottom member of the composite and was uniformly distributed over the entire sample area [23]. The current had to pass through the Lexan thermal barrier before passing through the top copper member and then entering the fluid. Results for $(T_i - T_0)/\Delta T$ obtained for runs 110918–110410 are shown as black symbols in figure D.1(a). Their average values are close to zero, showing that the radial temperature variation in the bottom plate was remarkably small and indeed negligible.
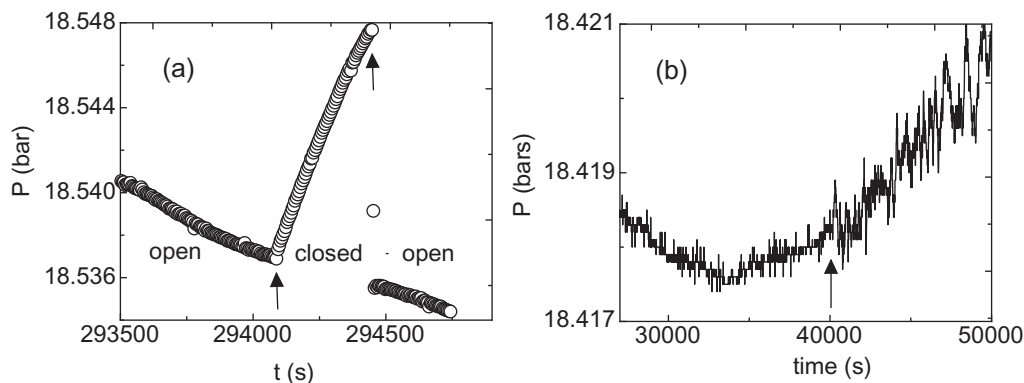
Figure E.1. (a) The sample pressure as a function of time. The data were taken on 14 September 2010, during a time interval when the Uboot temperature and pressure had not yet fully equilibrated. The sharp increase at the time indicated by the first arrow occurred when the valve was closed, and the sudden decrease at the second arrow was caused by opening the valve again. (b) The sample pressure as a function of time since the beginning of run 100918. Initially, the valve was open and the sample pressure could equilibrate with the Uboot pressure. When the valve was closed at $t = 40\,200$ s (the location of the arrow), the pressure could no longer equilibrate with the Uboot pressure and the fluctuations due to the turbulent convection became noticeable. This run is for $T_{\mathrm{m}} = 20.69\,^{\circ}$C, 18.4 bar, and $\Delta T = 11.37$ K, corresponding to $Ra = 9.25 \times 10^{14}$.

Appendix E. Evidence for a closed sample

HPCF-IIe was supposed to be completely sealed, except for a 2.5 cm diameter pipe entering it at half-height through the side wall. This pipe terminated outside the sample in a remotely operable valve which was to be open during an equilibration period to allow pressure equilibration between the Uboot and the sample, but closed when the system had reached a steady state after a new set point of the top- and bottom-plate temperatures had been established. In figure E.1(a) we show the pressure inside the sample during this equilibration period. With the valve open, the pressure of the Uboot and sample still drifted at a significant rate. In this case, however, the valve was closed prematurely. One can see that the sample pressure rose. When the valve was opened again, the pressure returned back to the Uboot pressure which all along had been drifting downward, albeit at a lesser rate. We regard this measurement as evidence that sealing the sample was indeed successful.

Figure E.1(b) shows the pressure with higher resolution after a steady state had been reached. With the valve open the noise level of the readings, reflecting the instrumental noise, is quite small but noticeable. After closing the valve, the noise level increases because the genuine noise in the pressure due to the turbulent convection in the sample becomes noticeable because it can no longer be smoothed out by an exchange of fluid with the Uboot. This phenomenon also indicates that sealing the sample was successful.

Table F.1. Effect of an SS temperature-deviation from the mean temperature for run 120415. $\langle T_{SS} \rangle$ is the set-point of the shield temperature. $T_{SS}(iL/4)$, $i = 1, 2, 3$, are the measured shield temperatures at the three vertical positions $iL/4$ as measured from the sample bottom.

Quantity	$\langle T_{SS} \rangle = T_m$	$\langle T_{SS} \rangle = T_m + 1\,K$
T_m	21.587	21.599
T_c	21.398	21.441
ΔT	10.163	10.191
$T_{SS}(L/4)$	21.629	22.621
$T_{SS}(2L/4)$	21.602	22.602
$T_{SS}(3L/4)$	21.550	22.571
Q (W)	320.6	319.6
Ra	6.70×10^{14}	6.76×10^{14}
Nu	4779	4747
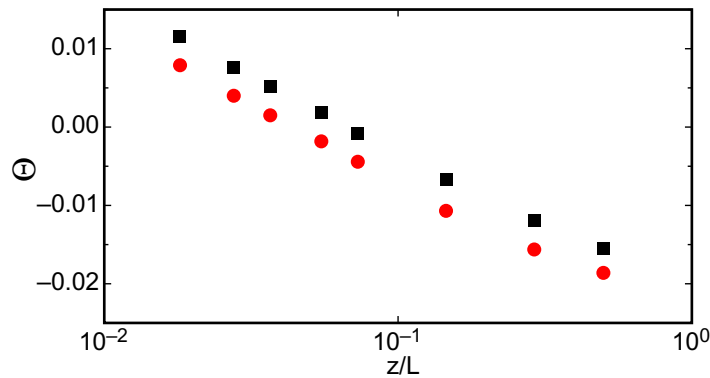
Figure F.1. The fluid temperature at a radial distance of 1 cm from the side wall as a function of the height z/L above the bottom of the sample. The red circles (black squares) are for $\langle T_{SS} \rangle = T_m$ ($\langle T_{SS} \rangle = T_m + 1\,K$).

Appendix F. Effect of side-shield mismatch with the sample temperature

As shown in figure 1, the side wall of the sample is surrounded by a side shield ('SS' in the figure) which is intended to prevent heat loss or input through the side wall. The temperature of this shield was controlled at the mean temperature T_m. Since the sample center temperature T_c will differ slightly from T_m due to non-Boussinesq effects, it is important to ask whether the heat input to the side wall due to the temperature difference $T_m - T_c$ is significant. Further, in view of the large size and mass of the shield, it is appropriate to ask how successful its temperature control was at a specified setpoint. Thus, a run was conducted in which the shield temperature was deliberately servoed at a displacement from T_m, which is much larger than $T_m - T_c$ or any deviations from perfect temperature regulation, namely at $T_m + 1.0\,K$. Various measured quantities with both setpoints are shown in table F.1. This example is for a nominal $\Delta T = 10.1\,K$.

First we call attention to the shield temperatures T_{SS} at the three vertical positions $L/4$, $L/2$, $3L/4$ (the sample height L was 2.2 m) measured from the bottom plate. They span a

vertical distance of over 1 m. One sees that the temperature gradient in the shield was typically about 0.05 K/m, which suggests that the shield temperature was uniform throughout within about 0.1 K.

A small shift of T_m and ΔT can be seen to have occurred due to the shift of the shield temperature by 1 K. This could happen because the bottom plate is a composite with a lower (BPb) and an upper (BPt) member (see figure F.1), with the temperature of BPb controlled. Thus the temperature of the BPt could adjust itself to prevailing heat currents and influence T_m as well as ΔT. The effect of a 1 K change in the shield temperature caused a change of 28 mK, or 0.3%, of ΔT and a shift of T_m by 12 mK. The effect of imperfect shield regulation on these quantities can be regarded as negligible.

The Rayleigh number was shifted by about 0.9%. This is due in part to the change of ΔT and in part due to a change of the fluid properties associated with the shift of T_m. Since actual temperature offsets are much less than 1 K, this effect is not serious. Similarly Nu is affected, by about 0.67%. This shift is due both to the change of ΔT and to a small change of the heat current needed to maintain the temperature of the bottom member of the bottom-plate composite (BPb) at the specified set-point. Again this is not a serious shift.

For completeness we also discuss the influence of the shield temperature on the sample temperature near the side wall. Although not directly relevant to this paper, it is important for other related investigations of temperature profiles in the bulk of the sample [42]. For that purpose, eight thermometers were mounted in the sample at a radial position 1 cm from the side wall and at eight vertical positions z_j. The eight temperatures $\Theta(z_j) \equiv [\langle T(z_j) \rangle - T_m]/(T_b - T_t)$ (we denote the time average by $\langle \ldots \rangle$) are shown in figure F.1 as a function of z/L. One sees that there is no change in the shape of the vertical temperature profile, but there is a small shift as had already been indicated by the shift of T_c shown in the table.

Finally we note that there are several other thermal shields in the system (see section 4), but we believe that their influence on the system performance is smaller than that of the SS.

Appendix G. Data tables

Table G.1. SF$_6$, HPCF-IIe, level sample (tilt angle $\beta < 0.0001$ rad).

Run no.	P (bar)	T_m (°C)	T_U (°C)	ΔT (K)	Ra	Pr	Nu
100918	18.419	20.691	23.777	11.370	$9.25II \times 10^{14}$	0.861	5507.45
100924	18.466	20.788	24.286	11.564	9.477×10^{14}	0.862	5579.63
100925	18.502	21.844	24.446	11.679	9.167×10^{14}	0.862	5447.81
101004	8.011	20.896	24.343	11.786	6.086×10^{13}	0.799	2145.55
101025	8.000	20.973	23.993	2.947	1.514×10^{13}	0.799	1371.90
101027	8.003	20.950	24.101	4.896	2.519×10^{13}	0.799	1616.40
101029	7.998	20.925	23.947	7.846	$4.03II \times 10^{13}$	0.799	1879.88
101031	8.005	20.895	24.160	11.786	6.075×10^{13}	0.799	2146.16
101102	8.016	20.870	24.549	17.732	9.179×10^{13}	0.799	2449.66
101114	11.751	20.977	24.611	13.447	2.063×10^{14}	0.820	3224.14
101116	11.762	21.021	24.849	20.030	3.079×10^{14}	0.821	3675.61
101108	14.891	20.920	25.015	17.826	6.060×10^{14}	0.842	4659.07
101109	14.894	21.247	25.008	18.479	$6.21II \times 10^{14}$	0.842	4694.89
101120	14.894	21.382	24.994	18.749	$6.27II \times 10^{14}$	0.842	4710.51
101122	14.843	21.498	24.246	11.988	3.945×10^{14}	0.841	4045.17

Table G.1. Continued.

Run no.	P (bar)	T_m ($^\circ$C)	T_U ($^\circ$C)	ΔT (K)	Ra	Pr	Nu
101124	14.810	21.272	23.786	7.938	$2.61\text{II} \times 10^{14}$	0.841	3526.58
101126	14.792	21.282	23.526	4.960	1.624×10^{14}	0.841	2995.86
101130	14.802	20.970	23.740	9.934	3.298×10^{14}	0.841	3814.08
101202	14.839	21.011	24.271	15.011	5.021×10^{14}	0.841	4382.99
101204	14.898	21.517	25.061	19.021	6.339×10^{14}	0.842	4724.05
101207	14.873	20.978	24.757	17.942	6.059×10^{14}	0.842	4661.48
101214	18.739	20.933	23.730	11.523	1.004×10^{15}	0.863	6154.13
101215	18.769	20.971	23.918	9.934	8.699×10^{14}	0.863	5410.40
101217	18.755	20.973	23.781	7.945	$6.93\text{II} \times 10^{14}$	0.863	4975.08
101218	18.814	21.644	24.306	12.274	1.051×10^{15}	0.863	5871.83
101219	18.817	21.612	24.295	11.214	9.620×10^{14}	0.863	5599.07
101221	18.812	21.536	24.246	10.065	8.657×10^{14}	0.863	5375.00
101223	18.785	21.566	23.998	9.125	7.785×10^{14}	0.863	5183.77
101225	18.781	21.583	23.960	8.160	6.949×10^{14}	0.863	4981.14
101227	18.751	21.490	23.682	6.975	5.924×10^{14}	0.863	4710.15
101229	18.709	21.432	23.289	0.861	7.258×10^{13}	0.863	1754.60
101231	18.740	21.483	23.570	5.961	5.051×10^{14}	0.863	4448.59
110102	18.735	21.487	23.522	4.971	4.205×10^{14}	0.863	4160.20

Table G.2. SF$_6$, HPCF-IIe, First tilted sample, tilt angle $\beta = 0.003$ rad.

Run no.	P (bar)	T_m ($^\circ$C)	T_U ($^\circ$C)	ΔT (K)	Ra	Pr	Nu
110115	4.181	20.950	23.734	4.896	5.176×10^{12}	0.787	966.79
110117	4.187	20.931	24.142	19.859	2.107×10^{13}	0.787	1497.77
110129	4.180	21.083	23.621	3.164	3.334×10^{12}	0.787	843.02
110131	4.187	20.930	24.159	19.858	2.107×10^{13}	0.787	1498.53
110202	4.184	20.855	23.987	13.708	1.455×10^{13}	0.787	1335.73
110204	4.184	20.895	23.947	9.791	1.038×10^{13}	0.787	1201.21
110206	4.185	20.938	24.046	5.875	6.228×10^{12}	0.787	1024.77
110221	18.565	21.040	24.198	12.067	1.001×10^{15}	0.862	5707.16
110227	18.574	21.034	24.286	12.057	$1.00\text{II} \times 10^{15}$	0.862	5716.32
110311	18.574	21.034	24.260	10.059	8.364×10^{14}	0.862	5302.69
110417	18.603	21.036	24.563	7.070	5.921×10^{14}	0.862	4694.05
110418	18.572	21.035	24.259	5.068	4.211×10^{14}	0.862	4133.38
110419	18.554	20.996	24.093	3.990	3.307×10^{14}	0.862	3758.72
110420	18.573	20.994	24.283	5.990	4.990×10^{14}	0.862	4412.69
110421	18.620	22.003	24.600	6.004	4.813×10^{14}	0.863	4374.31
110524	11.837	24.996	28.197	13.985	1.956×10^{14}	0.820	3157.24
110525	11.827	23.264	28.250	15.655	2.294×10^{14}	0.821	3336.36
110526	11.828	23.974	28.184	15.941	2.289×10^{14}	0.821	3331.77
110526	11.820	23.959	28.025	11.912	1.708×10^{14}	0.820	3023.89
110527	11.809	23.961	27.803	7.918	$1.13\text{II} \times 10^{14}$	0.820	2633.26

IOP Institute of Physics   **Φ** DEUTSCHE PHYSIKALISCHE GESELLSCHAFT

Table G.3. SF$_6$, HPCF-IIe, second tilted sample, tilt angle $\beta = 0.014$ rad.

Run No.	P (bar)	T_m (°C)	T_U (°C)	ΔT (K)	Ra	Pr	Nu
110625	4.971	24.017	27.841	1.033	1.533×10^{12}	0.789	661.28
110629	6.953	23.855	28.251	19.704	6.607×10^{13}	0.795	2178.61
110630	6.946	23.908	27.964	9.814	3.279×10^{13}	0.795	1744.85
110701	6.943	23.953	27.841	4.904	1.635×10^{13}	0.795	1395.79
110716	18.237	20.992	23.753	4.981	3.817×10^{14}	0.861	4011.57
110717	18.275	20.998	24.135	9.990	7.725×10^{14}	0.861	5162.00
110718	18.282	20.997	24.244	12.980	1.006×10^{15}	0.861	5707.97
110718	18.303	21.524	24.363	13.033	9.894×10^{14}	0.861	5629.48
110720	18.383	21.531	25.210	13.647	1.056×10^{15}	0.862	5790.57
110722	18.379	21.530	25.156	13.046	1.009×10^{15}	0.862	5673.03
110723	18.379	21.531	25.135	12.050	9.316×10^{14}	0.862	5496.51
110724	18.384	21.523	25.183	11.037	8.548×10^{14}	0.862	5323.81
110725	18.381	21.515	25.144	10.023	7.759×10^{14}	0.862	5144.72
110726	18.370	21.512	25.037	9.019	6.965×10^{14}	0.861	4950.18
110727	18.357	21.507	24.906	8.007	6.166×10^{14}	0.861	4741.89
110728	18.332	21.500	24.654	6.000	$4.59\text{II} \times 10^{4}$	0.861	4264.08
110731	18.340	21.498	24.760	4.993	3.830×10^{14}	0.861	3973.54
110801	18.323	21.004	24.672	5.004	3.916×10^{14}	0.861	3980.43
110802	18.341	21.001	24.848	6.997	5.501×10^{14}	0.861	4531.63
110803	18.339	21.261	24.791	5.520	4.281×10^{14}	0.861	4140.67
110803	16.166	21.475	24.995	5.945	2.696×10^{14}	0.850	3521.90
110804	16.168	21.475	25.014	5.946	2.697×10^{14}	0.850	3521.17
110805	16.173	21.467	25.078	8.431	3.831×10^{14}	0.850	3996.65
110806	16.182	21.473	25.197	11.937	5.435×10^{14}	0.850	4512.01
110807	14.105	21.649	24.915	6.295	1.720×10^{14}	0.836	3035.56
110808	14.105	21.650	24.909	6.291	1.719×10^{14}	0.836	3039.94
110809	14.113	21.742	25.037	8.982	$2.45\text{II} \times 10^{14}$	0.836	3431.72
110810	14.136	21.899	25.354	12.790	$3.49\text{II} \times 10^{14}$	0.836	3863.76
110811	12.061	21.453	25.045	5.906	9.694×10^{13}	0.822	2503.66
110812	12.060	21.454	25.034	5.908	9.695×10^{13}	0.822	2500.66
110813	12.065	21.442	25.135	8.380	1.378×10^{14}	0.822	2822.21
110814	12.067	21.434	25.177	11.861	1.951×10^{14}	0.822	3171.61
110815	12.078	21.445	25.383	16.879	2.784×10^{14}	0.823	3564.35
110816	12.101	21.673	25.806	21.336	3.515×10^{14}	0.823	3839.08
110817	12.077	21.437	25.356	6.872	1.133×10^{14}	0.823	2631.68
110824	10.068	21.454	25.455	5.404	5.161×10^{13}	0.810	2021.40
110625	10.068	21.440	25.457	6.877	6.570×10^{13}	0.810	2196.23
110626	10.063	21.425	25.319	8.846	8.440×10^{13}	0.810	2395.76
110827	8.013	21.510	25.143	9.017	4.593×10^{13}	0.799	1950.67
110828	8.010	21.444	25.047	5.885	2.999×10^{13}	0.799	1695.53
110829	8.013	21.454	25.137	4.908	2.503×10^{13}	0.799	1597.10
110911	5.025	21.422	25.492	6.604	1.060×10^{13}	0.789	1209.78
110912	5.023	21.390	25.369	9.779	1.568×10^{13}	0.789	1369.93
110913	5.023	21.372	25.387	12.240	1.964×10^{13}	0.789	1471.19
110914	5.020	21.407	25.206	8.205	1.314×10^{13}	0.789	1295.76

References

[1] Kadanoff L P 2001 Turbulent heat flow: structures and scaling *Phys. Today* **54** 34

[2] Ahlers G 2009 Turbulent convection *Physics* **2** 74

[3] Ahlers G, Grossmann S and Lohse D 2009 Heat transfer and large scale dynamics in turbulent Rayleigh–Bénard convection *Rev. Mod. Phys.* **81** 503

[4] Lohse D and Xia K-Q 2010 Small-scale properties of turbulent Rayleigh–Bénard convection *Annu. Rev. Fluid Mech.* **42** 335

[5] Kraichnan R H 1962 Turbulent thermal convection at arbitrary Prandtl number *Phys. Fluids* **5** 1374

[6] Spiegel E A 1971 Convection in stars *Annu. Rev. Astron. Astrophys.* **9** 323

[7] Castaing B, Gunaratne G, Heslot F, Kadanoff L, Libchaber A, Thomae S, Wu X Z, Zaleski S and Zanetti G 1989 Scaling of hard thermal turbulence in Rayleigh–Bénard convection *J. Fluid Mech.* **204** 1

[8] Chavanne X, Chillá F, Chabaud B, Castaing B, Chaussy J and Hébral B 1996 High Rayleigh number convection with gaseous helium at low temperature *J. Low Temp. Phys.* **104** 109

[9] Chavanne X, Chilla F, Castaing B, Hebral B, Chabaud B and Chaussy J 1997 Observation of the ultimate regime in Rayleigh–Bénard convection *Phys. Rev. Lett.* **79** 3648

[10] Niemela J J, Skrbek L, Sreenivasan K R and Donnelly R 2000 Turbulent convection at very high Rayleigh numbers *Nature* **404** 837

[11] Niemela J J, Skrbek L, Sreenivasan K R and Donnelly R 2000 Turbulent convection at very high Rayleigh numbers *Nature* **406** 439 (erratum)

[12] Chavanne X, Chilla F, Chabaud B, Castaing B and Hebral B 2001 Turbulent Rayleigh–Bénard convection in gaseous and liquid He *Phys. Fluids* **13** 1300

[13] Roche P E, Castaing B, Chabaud B and Hebral B 2001 Observation of the 1/2 power law in Rayleigh–Bénard convection *Phys. Rev.* E **63** 045303

[14] Roche P, Gauthier F, Chabaud B and Hébral B 2005 Ultimate regime of convection: robustness to poor thermal reservoirs *Phys. Fluids* **17** 115107

[15] Gauthier F and Roche P 2008 Evidence of a boundary layer instability at very high Rayleigh number *Eur. Phys. Lett.* **83** 24005

[16] Gauthier F, Salort J, Bourgeois O, Garden J, du Puits R, Thess A and Roche P 2009 Transition on local temperature fluctuations in highly turbulent convection *Euro. Phys. Lett.* **87** 44006

[17] Roche P-E, Gauthier F, Kaiser R and Salort J 2010 On the triggering of the ultimate regime of convection *New J. Phys.* **12** 085014

[18] Fleischer A and Goldstein R 2002 High-Rayleigh-number convection of pressurized gases in a horizontal enclosure *J. Fluid Mech.* **469** 1

[19] Niemela J J and Sreenivasan K R 2003 Confined turbulent convection *J. Fluid Mech.* **481** 355

[20] Niemela J J and Sreenivasan K R 2006 Turbulent convection at high Rayleigh numbers and aspect ratio 4 *J. Fluid Mech.* **557** 411

[21] Urban P, Musilová V and Skrbek L 2011 Efficiency of heat transfer in turbulent Rayleigh–Bénard convection *Phys. Rev. Lett.* **107** 014302

[22] He X, Funfschilling D, Bodenschatz E and Ahlers G 2012 Heat transport by turbulent Rayleigh–Bénard convection for $Pr \simeq 0.8$ and $4 \times 10^{11} \lesssim Ra \lesssim 2 \times 10^{14}$: ultimate-state transition for aspect ratio $\Gamma = 1.00$ *New J. Phys.* **14** 063030

[23] Ahlers G, Funfschilling D and Bodenschatz E 2009 Transitions in heat transport by turbulent convection for $Pr = 0.8$ and $10^{11} \leqslant Ra \leqslant 10^{15}$ *New J. Phys.* **11** 123001

[24] Ahlers G, Funfschilling D and Bodenschatz E 2011 Transitions in heat transport by turbulent convection for $Pr = 0.8$ and $Ra \lesssim 10^{15}$ *J. Phys.: Conf. Ser.* **318** 082001

[25] He X, Funfschilling D, Nobach H, Bodenschatz E and Ahlers G 2012 Transition to the ultimate state of turbulent Rayleigh-Beńard convection *Phys. Rev. Lett.* **108** 024502

[26] Ahlers G, Funfschilling D and Bodenschatz E 2011 Addendum: transitions in heat transport by turbulent convection for $Pr = 0.8$ and $10^{11} \leqslant Ra \leqslant 10^{15}$ *New J. Phys.* **13** 049401

[27] Ciliberto S, Cioni S and Laroche C 1996 Large-scale flow properties of turbulent thermal convection *Phys. Rev.* E **54** R5901

[28] Cioni S, Ciliberto S and Sommeria J 1997 Strongly turbulent Rayleigh–Bénard convection in mercury: comparison with results at moderate Prandtl number *J. Fluid Mech.* **335** 111

[29] Chillà F, Rastello M, Chaumat S and Castaing B 2004 Long relaxation times and tilt sensitivity in Rayleigh–Bénard turbulence *Eur. Phys. J.* B **40** 223

[30] Sun C, Xi H D and Xia K Q 2005 Azimuthal symmetry, flow dynamics, and heat transport in turbulent thermal convection in a cylinder with an aspect ratio of 0.5 *Phys. Rev. Lett.* **95** 074502

[31] Ahlers G, Brown E and Nikolaenko A 2006 The search for slow transients, and the effect of imperfect vertical alignment, in turbulent Rayleigh–Bénard convection *J. Fluid Mech.* **557** 347

[32] Oberbeck A 1879 Über die Wärmeleitung der Flüssigkeiten bei Berücksichtigung der Strömungen infolge von Temperaturdifferenzen *Ann. Phys. Chem.* **7** 271

[33] Boussinesq J 1903 *Theorie Analytique de la Chaleur* vol 2 (Paris: Gauthier-Villars)

[34] Niemela J and Sreenivasan K 2010 Does confined turbulent convection ever attain the 'asymptotic scaling' with 1/2-power? *New J. Phys.* **12** 115002

[35] Liu L and Ahlers G 1997 Rayleigh–Bénard convection in binary gas mixtures: thermophysical properties and the onset of convection *Phys. Rev.* E **55** 6950

[36] Grossmann S and Lohse D 2002 Prandtl and Rayleigh number dependence of the Reynolds number in turbulent thermal convection *Phys. Rev.* E **66** 016305

[37] Belmonte A, Tilgner A and Libchaber A 1994 Temperature and velocity boundary layers in turbulent convection *Phys. Rev.* E **50** 269

[38] Lui S L and Xia K-Q 1998 Spatial structure of the thermal boundary layer in turbulent convection *Phys. Rev.* E **57** 5494

[39] Tilgner A, Belmonte A and Libchaber A 1993 Temperature and velocity profiles of turbulence convection in water *Phys. Rev.* E **47** R2253

[40] Brown E and Ahlers G 2007 Temperature gradients and search for non-Boussinesq effects, in the interior of turbulent Rayleigh–Benard convection *Europhys. Lett.* **80** 14001

[41] Weiss S and Ahlers G 2011 Turbulent Rayleigh-Bénard convection in a cylindrical container with aspect ration $\Gamma = 0.50$ and Prandtl number $Pr = 4.38$ *J. Fluid Mech.* **676** 5

[42] Ahlers G, Bodenschatz E, Funfschilling D, Grossmann S, He X, Lohse D, Stevens R and Verzicco R 2012 Logarithmic temperature profiles in turbulent Rayleigh–Bénard convection *Phys. Rev. Lett.* **109** 114501

[43] Xu X, Bajaj K M S and Ahlers G 2000 Heat transport in turbulent Rayleigh-Bénard convection *Phys. Rev. Lett.* **84** 4357

[44] Ahlers G and Xu X 2001 Prandtl-number dependence of heat transport in turbulent Rayleigh–Bénard convection *Phys. Rev. Lett.* **86** 3320

[45] Xia K-Q, Lam S and Zhou S Q 2002 Heat-flux measurement in high-Prandtl-number turbulent Rayleigh–Bénard convection *Phys. Rev. Lett.* **88** 064501

[46] Funfschilling D, Brown E, Nikolaenko A and Ahlers G 2005 Heat transport by turbulent Rayleigh–Bénard convection in cylindrical cells with aspect ratio one and larger *J. Fluid Mech.* **536** 145

[47] Nikolaenko A, Brown E, Funfschilling D and Ahlers G 2005 Heat transport by turbulent Rayleigh–Bénard convection in cylindrical cells with aspect ratio one and less *J. Fluid Mech.* **523** 251

[48] Sun C, Ren L-Y, Song H and Xia K-Q 2005 Heat transport by turbulent Rayleigh–Bénard convection in cylindrical cells of widely varying aspect ratios *J. Fluid Mech.* **542** 165

[49] Grossmann S and Lohse D 2000 Scaling in thermal convection: a unifying view *J. Fluid Mech.* **407** 27

[50] Grossmann S and Lohse D 2001 Thermal convection for large Prandtl number *Phys. Rev. Lett.* **86** 3316

IOP Institute of Physics DEUTSCHE PHYSIKALISCHE GESELLSCHAFT

[51] Grossmann S and Lohse D 2004 Fluctuations in turbulent Rayleigh–Bénard convection: the role of plumes *Phys. Fluids* **16** 4462

[52] Ahlers G, Bodenschatz E, Funfschilling D and Hogg J 2009 Turbulent Rayleigh-Bénard convection for a Prandtl number of 0.67 *J. Fluid Mech.* **641** 157

[53] Brown E and Ahlers G 2007 Large-scale circulation model of turbulent Rayleigh–Bénard convection *Phys. Rev. Lett.* **98** 134501

[54] Brown E and Ahlers G 2008 A model of diffusion in a potential well for the dynamics of the large-scale circulation in turbulent Rayleigh–Bénard convection *Phys. Fluids* **20** 075101

[55] Zhou Q and Xia K-Q 2010 Measured instantaneous viscous boundary layer in turbulent Rayleigh–Bénard convection *Phys. Rev. Lett.* **104** 104301

[56] Stevens R J A M, Zhou Q, Grossmann S, Verzicco R, Xia K-Q and Lohse D 2012 Thermal boundary layer profiles in turbulent Rayleigh–Bénard convection in a cylindrical sample *Phys. Rev.* E **85** 027301

[57] Howard L N 1964 Heat transport in turbulent convection *J. Fluid Mech.* **17** 405

[58] Doering C and Constantin P 1996 Variational bounds on energy dissipation in incompressible flows: III convection *Phys. Rev.* E **53** 5957

[59] Lohse D and Toschi F 2003 The ultimate state of thermal convection *Phys. Rev. Lett.* **90** 034502

[60] Calzavarini E, Lohse D, Toschi F and Tripiccione R 2005 Rayleigh and Prandtl number scaling in the bulk of Rayleigh–Bénard turbulence *Phys. Fluids* **17** 055107

[61] Schmidt L E, Calzavarini E, Lohse D, Toschi F and Verzicco R 2012 Axially homogeneous Rayleigh–Bénard convection in a cylindrical cell *J. Fluid Mech.* **691** 52

[62] Boffetta G, Mazzino A, Musaccio S and Vozella L 2009 Kolmogorov scaling and Intermittency in Rayleigh-Taylor turbulence *Phys. Rev.* E **79** 065301R

[63] Shang X, Tong P and Xia K-Q 2008 Scaling of the local convective heat flux in turbulent Rayleigh–Benard convection *Phys. Rev. Lett.* **100** 244503

[64] Landau L D and Lifshitz E M 1987 *Fluid Mechanics* (Oxford: Pergamon)

[65] Grossmann S and Lohse D 2011 Multiple scaling in the ultimate regime of thermal convection *Phys. Fluids* **23** 045108

[66] von Kármán T 1930 Mechanische Ähnlichkeit und Turbulenz *Nachr. Akad. Wiss. Goett. II. Math.-Phys. Kl.* **58–76** 322

[67] Prandtl L 1932 Zur turbulenten Strömung in Rohren und laengs Platten *Ergeb. Aerodyn. Versuch, Göttingen* **IV** 18

[68] Marusic I, McKeon B J, Monkewitz P A, Nagib H M, Smits A J and Sreenivasan K R 2010 Wall-bounded turbulent flows at high Reynolds numbers: recent advances and key issues *Phys. Fluids* **22** 065103

[69] van Gils D P M, Huisman S G, Bruggert G-W, Sun C and Lohse D 2011 Torque scaling in turbulent Taylor–Couette flow with co- and counterrotating cylinders *Phys. Rev. Lett.* **106** 024502

[70] Huisman S G, van Gils D P M, Grossmann S, Sun C and Lohse D 2012 Ultimate turbulent Taylor–Couette flow *Phys. Rev. Lett.* **108** 024501

[71] Eckhardt B, Grossmann S and Lohse D 2000 Scaling of global momentum transport in Taylor–Couette and pipe flow *Eur. Phys. J.* B **18** 541

[72] Niemela J J and Sreenivasan K R 2006 The use of cryogenic helium for classical turbulence: promises and hurdles *J. Low Temp. Phys.* **143** 163

[73] Ahlers G 2000 Effect of sidewall conductance on heat-transport measurements for turbulent Rayleigh–Bénard convection *Phys. Rev.* E **63** R015303

[74] Roche P, Castaing B, Chabaud B, Hebral B and Sommeria J 2001 Side wall effects in Rayleigh Bénard experiments *Eur. Phys. J.* B **24** 405

[75] Funfschilling D, Bodenschatz E and Ahlers G 2009 Search for the 'ultimate state' in turbulent Rayleigh–Bénard convection *Phys. Rev. Lett.* **103** 014503

[76] Verzicco R 2004 Effect of non-perfect thermal sources in turbulent thermal convection *Phys. Fluids* **16** 1965

[77] Brown E, Nikolaenko A, Funfschilling D and Ahlers G 2005 Heat transport by turbulent Rayleigh–Bénard convection: effect of finite top- and bottom-plate conductivity *Phys. Fluids* **17** 075108

[78] Wu X Z 1991 *PhD Thesis* University of Chicago

[79] Stevens R J A M, Verzicco R and Lohse D 2010 Radial boundary-layer structure and Nusselt number in Rayleigh–Bénard convection *J. Fluid Mech.* **643** 495

[80] Niemela *et al* private communication

[81] Linden P F 1999 The fluid mechanics of natural ventilation *Annu. Rev. Fluid Mech.* **31** 201

[82] Wagner S, Shishkina O and Wagner C 2012 Boundary layers and wind in cylindrical Rayleigh–Bénard cells *J. Fluid Mech.* **697** 336

[83] Weiss S and Ahlers G 2012 Effect of tilting on turbulent convection: cylindrical samples with aspect ratio $\Gamma = 0.50$ *J. Fluid Mech.* submitted (arXiv:physics.flu-dyn/1206.1655)

[84] Ahlers G, Fontenele Araujo F, Funfschilling D, Grossmann S and Lohse D 2007 Non-Oberbeck–Boussinesq effects in gaseous Rayleigh–Bénard convection *Phys. Rev. Lett.* **98** 054501

[85] Ahlers G, Calzavarini E, Fontenele F, Araujo Funfschilling D, Grossmann S, Lohse D and Sugiyama K 2008 Non-Oberbeck–Boussinesq effects in turbulent thermal convection in ethane close to the critical point *Phys. Rev.* E **77** 046302

[86] Ahlers G, Brown E, Fontenele F, Araujo Funfschilling D, Grossmann S and Lohse D 2006 Non-Oberbeck–Boussinesq effects in strongly turbulent Rayleigh–Bénard convection *J. Fluid Mech.* **569** 409

[87] Brown E, Nikolaenko A and Ahlers G 2005 Reorientation of the large-scale circulation in turbulent Rayleigh–Bénard convection *Phys. Rev. Lett.* **95** 084503

[88] Brown E and Ahlers G 2006 Rotations and cessations of the large-scale circulation in turbulent Rayleigh–Bénard convection *J. Fluid Mech.* **568** 351